Master's thesis
Geophysics

Changes and variability of sea ice conditions in the Kara Sea

Iiro Kokkonen

May 2018

Supervisors: Jari Haapala and Andrea Gierisch

Reviewers: Petteri Uotila and Jari Haapala

UNIVERSITY OF HELSINKI
Institute for Atmospheric and Earth System Research

PL 64 (Gustaf Hällströmin katu 2a)
00014 Helsingin yliopisto

HELSINGIN YLIOPISTO — HELSINGFORS UNIVERSITET — UNIVERSITY OF HELSINKI

Tiedekunta — Fakultet — Faculty	Laitos — Institution — Department
Faculty of Science	INAR

Tekijä — Författare — Author
Iiro Kokkonen

Työn nimi — Arbetets titel — Title
Changes and variability of sea ice conditions in the Kara Sea

Oppiaine — Läroämne — Subject
Geophysics

Työn laji — Arbetets art — Level	Aika — Datum — Month and year	Sivumäärä — Sidoantal — Number of pages
Master's thesis	May 2018	72 pages

Tiivistelmä — Referat — Abstract

The Kara Sea is part of the seasonal sea ice zone in the Arctic, where the warming climate is rapidly changing the sea ice regime. The warm Atlantic water transported through the Barents Sea has a strong influence on the ice conditions in the northern Kara Sea.

In this thesis, trends and interannual variability in sea ice conditions in the Kara Sea area studied. For this purpose, coupled sea ice–ocean model NEMO-LIM3 and sea ice concentration datasets derived from passive microwave satellite observations (SMMR, SSM/I and SSMIS) are used. Additionally, the model performance is assessed by comparing its output with the observations.

The ice coverage examined in regional and local scales shows negative trends in all months in 1978–2015. The interannual variability of the total ice covered fraction increased in winter and spring when the ice regime shifted from full to partial ice cover over the sea. Meanwhile the variability in summer and autumn decreased. The annual ice free time rapidly extended in the area north of Novaya Zemlya where the warm Atlantic water enters the Kara Sea. The mean sea ice thickness, based on the sea ice–ocean model data in 1997–2015, has become thinner in all months. The model is generally in good agreement with the observations, with the exception of the northern Kara Sea where the model underestimated heat advection. The findings confirm that the sea ice conditions in the Kara Sea have changed towards a new regime with shorter and more variable ice seasons.

Avainsanat — Nyckelord — Keywords
Sea ice, Kara Sea, modeling, changes, interannual variability

Säilytyspaikka — Förvaringsställe — Where deposited
Kumpula campus library

Muita tietoja — övriga uppgifter — Additional information

HELSINGIN YLIOPISTO — HELSINGFORS UNIVERSITET — UNIVERSITY OF HELSINKI

Tiedekunta — Fakultet — Faculty	Laitos — Institution — Department
Matemaattis-luonnontieteellinen tiedekunta	INAR

Tekijä — Författare — Author
Iiro Kokkonen

Työn nimi — Arbetets titel — Title
Changes and variability of sea ice conditions in the Kara Sea

Oppiaine — Läroämne — Subject
Geofysiikka

Työn laji — Arbetets art — Level	Aika — Datum — Month and year	Sivumäärä — Sidoantal — Number of pages
Pro Gradu -tutkielma	Toukokuu 2018	72 sivua

Tiivistelmä — Referat — Abstract

Karanmeri kuuluu arktiseen vuodenaikaisen merijään vyöhykkeeseen, missä lämpenevä ilmasto muuttaa nopeasti vallitsevia merijääolosuhteita. Pohjoisella Karanmerellä Barentsin meren läpi kulkeutuvalla lämpimällä Atlantin vedellä on suuri vaikutus merijääoloihin.

Tutkielman tarkoituksena on tutkia muutoksia ja vuosien välistä vaihtelua Karanmeren jääoloissa. Tutkimuksessa hyödynnetään kytkettyä NEMO-LIM3 merijää-merimallia sekä satelliittihavainnoista (SMMR, SSM/I ja SSMIS instrumentit) johdettuja merijään peittävyys aineistoja. Lisäksi mallin toimivuutta arvioidaan vertailussa havaintojen kanssa.

Jään peittävyydessä havaittiin negatiivinen trendi vuoden jokaisena kuukautena välillä 1978–2015. Vaihtelevuus jään peittämässä alassa kasvoi talvella ja keväällä, jolloin jää ei enää peitä koko Karanmerta. Vastaavasti kesäaikana vaihtelevuus pieneni. Vuoden jäätön aika kasvoi nopeasti Novaja Zemljan pohjoispuolisella alueella, jonne virtaa lämmintä vettä Barentsin mereltä. Jäämalliin perustuva keskimääräinen jään paksuus välillä 1997–2015 pieneni kaikkina kuukausina. Jäämallin tulokset ovat yleisesti yhteneviä havaintojen kanssa. Malli kuitenkin aliarvioi lämmönkuljetusta pohjoiselle Karanmerelle. Tulokset vahvistavat Karanmeren jääpeitteisten kausien muuttuneen lyhytkestoisemmiksi ja vaihtelevammiksi.

Avainsanat — Nyckelord — Keywords
Merijää, Karanmeri, mallinnus, muutokset, vuosien välinen vaihtelu

Säilytyspaikka — Förvaringsställe — Where deposited
Kumpulan kampuskirjasto

Muita tietoja — övriga uppgifter — Additional information

Contents

1 Introduction **1**

1.1 The Kara Sea 1

1.2 Sea ice decline in the Kara Sea 4

1.3 Importance of sea ice in the Kara sea 6

1.4 Outline of the thesis 8

2 Drivers of the sea ice conditions **9**

2.1 Basic sea ice equations 9

2.1.1 Ice dynamics 9

2.1.2 Ice state and conservation 11

2.1.3 Mechanical redistribution 12

2.1.4 Thermodynamics 12

2.1.5 Salinity of sea ice 16

2.2 Oceanic and atmospheric drivers and indexes 17

2.2.1 Arctic warming and feedbacks 17

2.2.2 The atmospheric and ocean circulation in the Kara Sea 19

2.2.3 Effects of large scale atmospheric oscillations on the sea ice . . 22

3 Data and methods **25**

3.1 NEMO-LIM3 25

3.2 Satellite observation datasets 27

3.3 Methods 29

4 Results **32**

4.1 Monthly mean ice concentration 33

4.2 Ice covered fraction trends and variability 36

4.3 Ice covered fraction in subregions 40

4.4 Ice thickness 46

4.5 Ice free time 47

5 Discussion **54**

6 Conclusions **61**

Acknowledgements **63**

Bibliography **64**

1. Introduction

1.1 The Kara Sea

The region under investigation in this Master's thesis is the Kara Sea, a marginal sea of the Arctic Ocean. The Kara Sea is located north of Siberia and is entirely north of the polar circle. Figure 1.1 shows a map of the Kara Sea with the most important geographical features labeled. The Kara Sea is rather isolated from adjacent seas. Novaya Zemlya islands and Severnaya Zemlya archipelago separate the region from the Barents and Laptev Seas, respectively. The southern and eastern parts of the Kara Sea are connected to adjacent seas only by relatively narrow and shallow straits, while the northern half of Kara Sea is more open to the Arctic Ocean and the northern Barents Sea. In the south the Kara Sea is bounded by the Siberian coastline including the widespread estuaries of Ob and Yenisei rivers. Most of the sea is located on the coastal shelf zone and the average depth of the whole sea is only 111 meters. In the small straits water transport is limited by bathymetry (*Volkov et al.*, 2002, pp. 30–36). The deepest parts in the northeast allow water inflow in deeper layers from the Barents Sea and the Arctic Ocean.

Ob and Yenisei are some of the biggest rivers in the world. Along with a number of other rather large rivers, they bring a significant fresh water inflow to the Kara Sea. Relative to the sea's area, the mean annual freshwater inflow into the Kara Sea is the largest in world (*Volkov et al.*, 2002, p. 37). Because of the fresh

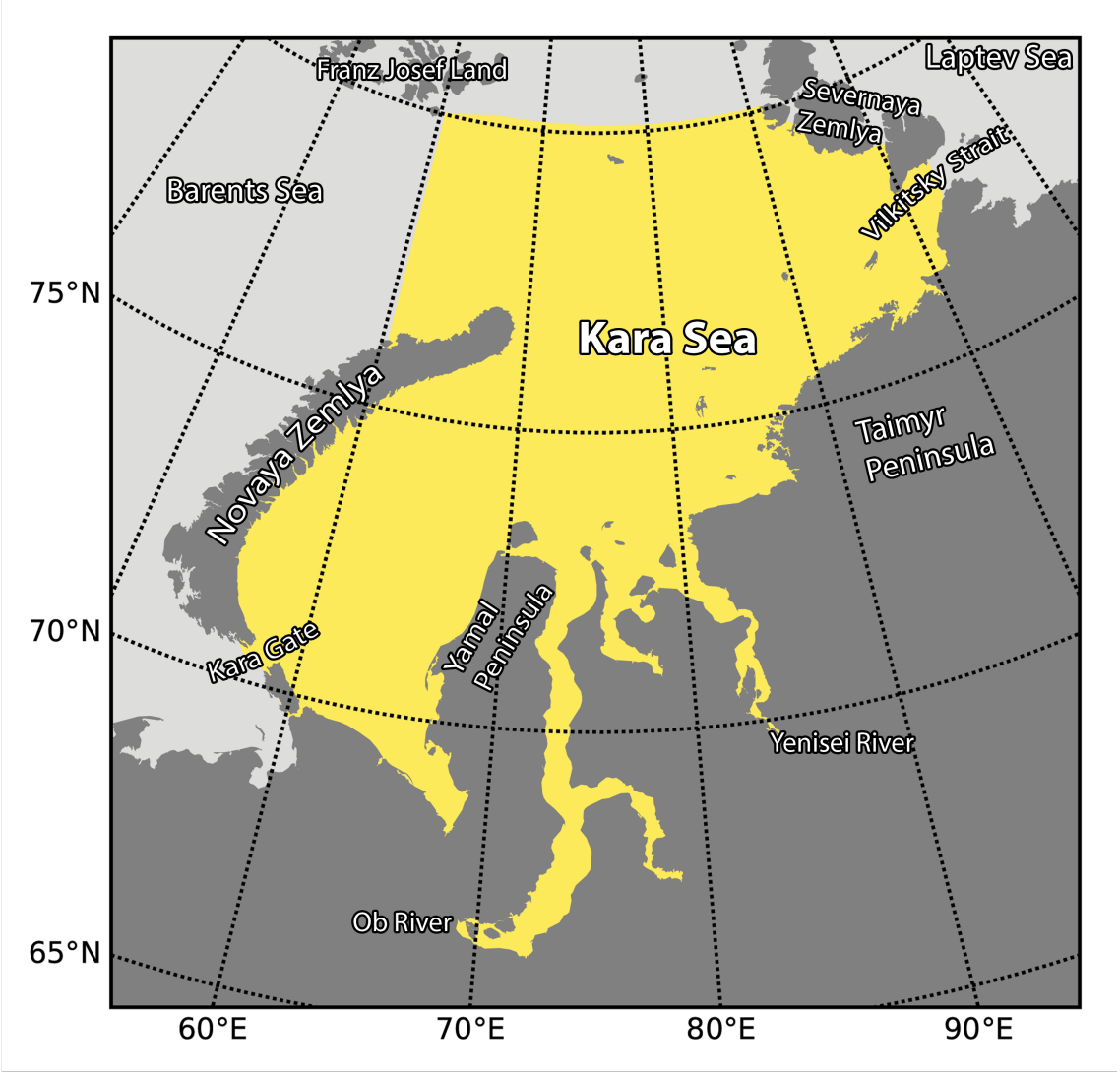

Figure 1.1: The Kara Sea.

water inflow combined with the blockages to saline Atlantic water flow, the salinity of the Kara Sea is low. The salinity is highest near Kara Gate and north of Novaya Zemlya where saline Atlantic water enters from the Barents Sea.

Ice formation in the Kara Sea starts in the north, close to the Arctic Ocean, where some ice may have survived over the summer. The ice edge progresses southward faster in the eastern part of the sea, where heat content and salinity in the water are lower. Stable ice cover is formed last near the northern tip of Novaya Zemlya and around Kara Gate strait. Usually the sea remains ice covered from late

November until May. The ice break-up starts from Yenisei and Ob estuaries. The break-up process is accelerated by inflow of warm water from the Barents Sea and from the rivers. At the end of the melting season in September the minimum ice extent is reached (*Volkov et al.*, 2002, pp. 308–309).

Fast ice or landfast ice is the part of the sea ice cover that is attached to shore and remains stationary. Fast ice in the Kara sea has been of special interest in many studies (*Divine et al.*, 2003, 2004, 2005; *Olason*, 2016). In wintertime there are extensive fast ice formations along the coastal zone of the Kara Sea. The fast ice is held in place in shallow areas by grounded ice ridges. The great number of islands allows the extension of fast ice also into the deeper water areas, because the ice floes are stabilized between islands by internal mechanics of the ice pack. The phenomenon is called arching (*Olason*, 2016). Significant variation in fast ice extent annually and seasonally has been noticed depending on winter temperatures, direction of winds and cyclonic activity (*Divine et al.*, 2003). Wide fast ice formations are challenging to ships as they often block access to straits and ports.

Ice drift direction in the open sea is mainly governed by wind, ocean currents and the Coriolis effect. In coastal areas ice drift direction is also affected by coasts and shallows. Like all Arctic shelf seas, the Kara Sea is a net exporter of sea ice to the Arctic Ocean (*Kern et al.*, 2005). The mean drift velocity in the Kara Sea reported by *Volkov et al.* (2002) is 8.5 km/day, but locally about one magnitude higher velocities are possible in straits (*Volkov et al.*, 2002, p. 344). Converging ice drift leads to the formation of ridges. Their concentration is greater in the northern Kara Sea, where interaction with old and thick Arctic ice is common. High concentration of ridges can also be found near straits and around capes and islands (*Volkov et al.*, 2002, p. 339).

Polynyas occur frequently along the edge of fast ice zones from the northeastern Kara Sea to north of Ob and Yenisei estuaries, around Yamal Peninsula to Kara

Gate as well as on the coasts of Novaya Zemlya (*Johannessen et al.*, 2006, p. 270). In the Kara Sea polynyas are mostly created by offshore winds. The inter-annual variability of winds also makes polynyas prone to inter-annual variability. Polynyas are important for new ice production in the winter and they are regions of convection and formation of saline deep water (*Volkov et al.*, 2002, pp. 324–325). During the melting season polynyas are good absorbers of heat, and ice melts quickly around them. In the wintertime, long polynyas roughly parallel to coasts can serve as excellent shipping routes.

1.2 Sea ice decline in the Kara Sea

In many Arctic-wide studies the Kara Sea and Barents Sea regions are among the top contributors to the negative trends of Arctic sea ice extent (*Cavalieri and Parkinson*, 2012; *Chen et al.*, 2016). In *Chen et al.* (2016) regional ice extent trends from 1979 to 2014 were examined. In the Kara and Barents Seas the trend in September/October was -20.1%/decade and in November/December -10.7%/decade. The decline was accelerating in later years and the inter-annual variability of sea ice extent in wintertime had increased.

The swift regime change in the Barents and Kara Seas is anticipated, because they are located at the current edges of the seasonal marginal ice zone and are therefore the 'next in line' to experience a loss of sea ice, when climate warms. Atmospheric temperatures in the Arctic have quickly increased (*Screen and Simmonds*, 2010). Various feedback effects related to changes in heat fluxes and surface albedo can amplify the warming in the Arctic. Poleward shift of the Gulf Stream in the North Atlantic and changes in large scale atmospheric circulation associated with it could explain quick climate warming in the Barents and Kara Seas region (*Sato et al.*, 2014). Changes in storm track can lead to and increase of atmospheric heat advection to the Kara Sea region (*Jung et al.*, 2017). The ice conditions in

the Barents and Kara Seas are greatly dependent on the inflow of warm Atlantic water (*Hanzlick and Aagaard*, 1980; *Årthun et al.*, 2012). The warm Atlantic water inflow has had a great effect on variations and decline of the sea ice cover in the Barents Sea (*Onarheim et al.*, 2015; *Onarheim and Årthun*, 2017; *Li et al.*, 2017). In the Kara Sea the heating effect of Atlantic inflow is significant, but limited by the blocking effect of Novaya Zemlya (*Hanzlick and Aagaard*, 1980). Since the rate of decline in the Barents Sea ice cover has been fastest in the northeast near the edges of the Kara Sea, and the decline is expected to continue (*Onarheim and Årthun*, 2017), big changes in the ice conditions of the Kara Sea are more than likely.

The decline of sea ice can also be seen in the length of the ice free season. The length of the ice free season is a useful measure for the sea ice cover evolution in a given location or in a small region and it is also a meaningful quantity for example for ships. *Rodrigues* (2008) discovered that the ice free season is extending in large scale everywhere in the Arctic. Lengthening of the ice free season was also detected in the Kara Sea at a rate of 1.3 days/year in 1979–2006, accelerating to 8.2 days/year in 2001–2007 (*Rodrigues*, 2009).

In regional inspection ice concentrations have been found to be decreasing all over the Kara Sea. According to *Rodrigues* (2008) the decline has been fastest in the western Kara Sea, where about 57% of the ice was lost between years 1979 and 2006. Especially summer ice extents have dropped significantly but vary greatly from year to year. The change was less prominent in wintertime. The east coast of Novaya Zemlya was one of the few regions of the Russian Arctic where the ice free time had shortened since 1979. The ice free time in the Vilkitsky and Shokalsky straits remained short, but has increased. The extent of fast ice has decreased in the biggest continuous formation in the Kara Sea on the coast of Taimyr Peninsula (*Divine et al.*, 2003). All in all the ships navigating the sea today can with great probability expect easier ice conditions than thirty years ago (*Rodrigues*, 2008).

The decline of sea ice in the Kara Sea is in big picture connected to the decline of Arctic sea ice. Sea ice in the Arctic has receded in the recent decades. The extent of sea ice has been studied using data from satellite based instruments. The ice extent in the Arctic has been in decline in all months (*Serreze et al.*, 2007; *Cavalieri and Parkinson*, 2012). The fastest decline is taking place in summer months (*Barber et al.*, 2017, pp. 105–106). The interannual variability of the Arctic ice extent has been high (*Cavalieri and Parkinson*, 2012; *Simmonds*, 2015). In the past decade multiple reports of record low ice extent and accelerating decline have been made (*Comiso et al.*, 2008; *Stroeve et al.*, 2011; *Overland and Wang*, 2013; *Simmonds*, 2015). The length of the open water season and the whole thermodynamics of the Arctic sea ice cover is changing (*Barber et al.*, 2017, p. 107, 112–114).

The declining ice extent is accompanied by decline of thick multi-year ice (e.g. *Comiso*, 2012). Loss of multi-year ice is associated with the decrease of sea ice extent, since thinner first year ice is faster to melt (*Stroeve et al.*, 2011).

Loss of multi-year ice is leading to general thinning of the Arctic sea ice. The thinning has been observed from submarine based measurements (*Rothrock et al.*, 1999) and later from satellite measurements (e.g. *Kwok et al.*, 2009). The thickness distribution in the Arctic has shifted toward generally thinner ice thicknesses (*Oikkonen and Haapala*, 2011). Changes in Arctic-wide distribution of ice thickness and in the decline of ice extent have been associated also with increased sea ice drift speed (*Rampal et al.*, 2009; *Barber et al.*, 2017, pp. 117–118).

1.3 Importance of sea ice in the Kara sea

Besides basic research, information about sea ice is required for operational and strategical planning by shipping industry and other off-shore operations (*Johannessen et al.*, 2006, p. 123). Decision about the ship's route depends on the ice conditions with the goal set to minimize travel time, fuel consumption and risk of

accidents. Current ice conditions for the ships are provided in form of ice charts and satellite images. For the purpose of planning routes in advance, estimating near future ice conditions is vital. Forecasting of ice conditions is based on simulating the evolution of the ice cover with ice models. For the needs of shipping, the information about ice thickness, concentration and type are the most important (*Lei et al.*, 2015).

The Northern Sea Route (NSR) traverses Kara Sea. While the route from Central Europe to Far East Asia via the NSR is up to 40% shorter than the southern route through Suez Canal, the cargo volume transported through NSR remains comparatively small (*Buixadé Farré et al.*, 2014). The variable and harsh ice conditions and shallow straits lower the attractiveness of the route. With changing ice conditions the route is becoming more accessible and traffic volume is expected to increase (*Khon et al.*, 2017; *Buixadé Farré et al.*, 2014). Beside transit traffic on the NSR, there is potential for traffic to destinations in northern Siberia. Plans have been made to exploit the considerable oil, natural gas and strategic metal reserves in the Kara Sea region (*Johannessen et al.*, 2006, p. 423). One realized project that is expected to contribute to the increase in the Kara Sea traffic is a new liquefied natural gas plant about to be opened at Sabetta on the Yamal Peninsula along with a new sea port (*Buixadé Farré et al.*, 2014).

Increasing human activity on the sea, combined with difficult ice conditions, leads to increased risk of accidents with a possibility of losing human lives and damaging the environment. A ship stuck in ice pack can uncontrollably drift into shallow waters and ground. A compressing ice field poses a risk of tilting the ship and it can even cause hull damage under high pressure. Hull damage to oil tankers can cause major oil spills and ecological disaster.

1.4 Outline of the thesis

The goal of this thesis is to examine the changes and variability of the ice cover in the Kara Sea. For this purpose the coupled sea ice–ocean model NEMO-LIM3 and passive microwave satellite observations are used. The NEMO-LIM3 model setup for the Kara Sea is still unvalidated. The model's accuracy in a hindcast run is tested in this thesis by comparing sea ice variables of the model against those of the satellite based datasets.

The introduction of this Master's thesis in Section 1 contains a literature review about changes in sea ice conditions in the Kara Sea. The study area is defined and special oceanographic details of Kara Sea are presented. The importance of sea ice for shipping activity is described. Section 2 introduces the basic equations and phenomena of sea ice physics as well as the factors driving variability and changes in sea ice conditions. In Section 3 the NEMO-LIM3 sea ice–ocean model and the satellite datasets and methods used in this study are presented. Some specific methods used in the analysis are described in detail. Section 4 contains the results about changes and variability in the sea ice conditions in the Kara Sea obtained by the analyses. The results from the model data and observation based data are compared. Section 5 contains the discussion about the obtained results and Section 6 contains the concluding remarks of this Master's thesis.

2. Drivers of the sea ice conditions

2.1 Basic sea ice equations

Sea ice models commonly treat sea ice as a continuum. Sea ice models solve the basic sea ice equations in order to simulate the physical behavior of the ice cover. These equations describe the evolution of the ice cover as the result of several dynamic and thermodynamic processes. The evolution of sea ice cover is governed by atmospheric and ocean forcing.

2.1.1 Ice dynamics

Momentum balance

The momentum balance that is used to solve the velocity vector of sea ice $\mathbf{u}$ can be expressed as (*Rousset et al.*, 2015)

$$m\frac{D\mathbf{u}}{Dt} = A\left(\boldsymbol{\tau}_a + \boldsymbol{\tau}_w\right) - mf\mathbf{k}\times\mathbf{u} - mg\nabla\eta + \nabla\cdot\sigma, \tag{2.1}$$

where m is the mass of ice and snow, A is the ice concentration, $\boldsymbol{\tau}_a$ is the atmospheric stress vector from wind forcing and $\boldsymbol{\tau}_w$ the water stress vector from sea surface currents, f is the Coriolis parameter, $\mathbf{k}$ is an up pointing unit vector, g is the acceleration of gravity and η is the sea surface elevation. The last term, $\nabla\cdot\sigma$, represents the internal stress of the ice pack. The internal stress of the ice pack is related to the mechanical interactions of the ice pack and it is dependent on rheology.

Rheology and internal stress

Rheology describes how the stress in a medium is related to the material properties and strain rate. The rheology defines a formula for the stress tensor σ as a function of strain ϵ, strain rate $\dot{\epsilon}$, and material properties included in ice state variables. Some basic rheological models include linear elastic, linear viscous and ideal plastic (*Leppäranta*, 2011, p. 109). More complex models can have nonlinearities and can be combine properties of many different models.

The most widely used rheology in sea ice models is the viscous-plastic rheology with elliptical yield curve (*Hibler III*, 1979). The plastically deforming nature of sea ice can be seen in formation of leads and ridges while the viscous behavior is apparent in large scale ice flow.

For viscous rheology the strain rate tensor and invariants are defined:

$$\dot{\epsilon} = \begin{bmatrix} \dot{\epsilon}_{11} & \dot{\epsilon}_{12} \\ \dot{\epsilon}_{21} & \dot{\epsilon}_{22} \end{bmatrix}, \tag{2.2}$$

from which the first and second strain rate invariants are defined as:

$$\dot{\epsilon}_I = \dot{\epsilon}_{11} + \dot{\epsilon}_{22}, \tag{2.3}$$

$$\dot{\epsilon}_{II} = \sqrt{(\dot{\epsilon}_{11} + \dot{\epsilon}_{22}) + 4\dot{\epsilon}_{12}^2}. \tag{2.4}$$

The stress tensor and invariants are defined similarly. The constitutive law of the viscous plastic rheology is formulated as (*Hibler III*, 1979):

$$\sigma = 2\eta\dot{\epsilon}_{ij} + [\zeta - \eta]\,\dot{\epsilon}_I\delta_{ij} - (P/2)\,\delta_{ij}. \tag{2.5}$$

$\dot{\epsilon}$ is the sea ice strain rate tensor and $\dot{\epsilon}_I$ is first strain rate invariant, equal to the divergence rate. $P/2$ is the pressure term, which includes the connection to ice thickness and concentration. δ is the Kronecker delta. ζ and η are the nonlinear bulk and shear viscosities, respectively. The nonlinear viscosities are formulated as

$$\eta = \zeta/e^2, \tag{2.6}$$

$$\zeta = P/2\sqrt{\dot{\epsilon}_I^2 + \dot{\epsilon}_{II}^2/e^2}, \tag{2.7}$$

where e is the ratio of compressive strength and shear strength.

The yield curve of viscous-plastic rheology determines the nature of flow under applied stress. Yield curves are commonly presented in a plane spanned by the principal stresses (*Leppäranta*, 2011, p. 122). The principal stresses are $\sigma_1 = \sigma_I - \sigma_{II}$ and $\sigma_2 = \sigma_I + \sigma_{II}$. Stresses inside the yield curve cause viscous flow while stresses on the yield curve cause plastic deformation. The surface inside the curve in *Hibler III* (1979) viscous plastic rheology is elliptic with ratio of elliptic axes equal to e. The elliptic yield curve allows ice to strongly resist compression and shear, but the ice pack lacks tensile strength.

2.1.2 Ice state and conservation

For modeling sea ice an ice state must be defined. A common approach is using the ice thickness distribution for ice state (*Leppäranta*, 2011, p. 62). For modeling purposes the ice thickness distribution is discretized into ice thickness categories.

For each thickness category ice state variables are defined, which include for example the mean thickness, volume, concentration, salinity and enthalpy. Changes to ice state variables arise from transport, thermodynamics, and mechanical redistribution processes. The effect of these processes to an ice state variable is described by a conservation equation of the form (*Vancoppenolle et al.*, 2009)

$$\frac{\partial X}{\partial t} = -\nabla \cdot (X\mathbf{u}) + \Psi^X + \Theta^X, \tag{2.8}$$

where the term $-\nabla \cdot (X\mathbf{u})$ represents advection, Ψ^X is the mechanical redistribution function and Θ^X is the thermodynamic redistribution function of ice state variable X. The redistribution functions are presented more in detail in Sections 2.1.3 and 2.1.4.

2.1.3 Mechanical redistribution

In the sea ice conservation equations the effects of sea ice deformations, such as ridging and lead opening, are expressed in the mechanical redistribution function. A general expression of mechanical redistribution functions Ψ^X was proposed by *Thorndike et al.* (1975):

$$\Psi^X = \left(\dot{\epsilon}_1^2 + \dot{\epsilon}_{11}^2\right)^{1/2} \left\{\alpha_0\left(\theta\right) w_o + \alpha_r\left(\theta\right) w_d\right\}. \tag{2.9}$$

$\dot{\epsilon}_1$ and $\dot{\epsilon}_{11}$ are the strain rate tensor invariants, α_0 and α_r are constants related to lead opening and closing rates and $\theta = \arctan(\dot{\epsilon}_{11}/\dot{\epsilon}_1)$. w_o and w_d are the opening and deforming modes respectively.

The deforming mode includes deformations by ridging and rafting. In general thinner ice has a tendency to raft while thicker ice is more likely to form ridges as a result of convergence. Deformation by rafting produces ice with double the thickness of participating ice. Ridging results in the participating ice being distributed to a range of ice thicknesses. The equation of deformation mode is (*Vancoppenolle et al.*, 2009)

$$w_d\left(h, g\right) = -\left[b^{ra}\left(h\right) + b^{ri}\left(h\right)\right] g\left(h\right) + n^{ra}\left(h\right) + n^{ri}\left(h\right), \tag{2.10}$$

where $b^{ra}(h)$ is the rafting participation function and $b^{ri}(h)$ is the ridging participation function. The participation functions determine the areas of the ice thickness space that experience deformations, usually defined so that only the thinnest part in the ice thickness space deforms. The last two terms are the transfer functions for rafting and ridging ice. Thin ice deforms in rafting mode and if the participating ice thickness exceeds a certain threshold thickness, the ice will form ridges.

2.1.4 Thermodynamics

The thermodynamic redistribution function includes all changes in the sea ice caused by thermodynamic processes. The thermodynamic formation and evolution of sea

ice is driven by energy balance at atmospheric and ocean interfaces of the sea ice and heat transfer inside the ice.

Heat conduction and transfer

The basal and surface heat fluxes of sea ice are connected by heat conduction through ice and snow:

$$F_c(z) = -\lambda_{si}\left(\frac{\partial T}{\partial z}\right)_z. \tag{2.11}$$

The heat flux at depth z in the ice is controlled by the sea ice thermal conductivity λ_{si} and the local temperature gradient, $\frac{\partial T}{\partial z}$, where z is the depth from ice surface (*Petrich and Eicken*, 2016, p. 21). The thermal conductivity is a function of temperature as well as of brine and gas fractions in the ice. For snow cover on top of ice, a similar equation is applied. The thermal conductivity of snow is generally lower compared to ice, which means snow acts as an insulator on top of ice slowing down the ice growth. Since the temperature at the ice base is at the freezing point, the heat conduction is heavily governed by the surface energy balance (*Petrich and Eicken*, 2016, p. 33).

The propagation of heat into sea ice with internal heat source from shortwave radiation absorption follows the heat transfer equation

$$\rho_i c_{si}\frac{dT}{dt} = \lambda_{si}\frac{\partial^2 T}{\partial z^2} + \kappa I_0 \exp(-\kappa z), \tag{2.12}$$

where ρ_i is the density of ice, c_{si} is the specific heat capacity, κ is the extinction coefficient of radiation in sea ice and I_0 is the solar radiation penetrating the ice surface.

Surface energy balance

The heat balance at sea–atmosphere interface is shown in Equation 2.13 (*Persson and Vihma*, 2016, p. 161):

$$F_{atm} = SW_d - SW_u + LW_d - LW_u - H_s - H_l. \tag{2.13}$$

The surface energy balance, F_{atm}, includes terms for downward and upward shortwave (SW_d and SW_u) radiation and longwave (LW_d and LW_u) radiation fluxes. The term H_s is the sensible heat flux and H_l is the latent heat flux.

The downward shortwave radiation flux from the sun varies depending on the season and time of the day. Part of the radiation is absorbed and reflected already in the atmosphere especially by clouds. Shortwave radiation is also transmitted through ice and is absorbed below surface. The upward shortwave radiation flux is the reflected part of incoming solar radiation. It depends on the surface albedo, which varies greatly spatially and temporally even in short scales.

The atmosphere emits longwave radiation downward depending on humidity, cloudiness and temperature of the atmosphere. Similarly, longwave radiation is emitted upward to the atmosphere by the surface depending on the surface temperature and emissivity.

The turbulent heat fluxes at the atmospheric interface are the sensible heat flux, associated with temperature difference between atmosphere, and the ice surface and the latent heat flux, associated with evaporation and sublimation at the surface. The magnitude and direction of turbulent fluxes depends on surface characteristics like temperature, moisture and roughness as well as on atmospheric properties such as temperature, humidity, wind speed and atmospheric stratification.

In closer inspection the surface heat balance equation (Eq. 2.13) is formulated (*Persson and Vihma*, 2016, p. 161):

$$\begin{aligned} F_{atm} =& SW_d\,(1-\alpha) + (1-\varepsilon)LW_d - \varepsilon\sigma T_s^4 \\ & - \rho_a c_p C_H U\,(T_s - T_a) - \rho_a L_v C_v U\,(Q_s - Q_a)\,. \end{aligned} \tag{2.14}$$

where α is the ice albedo, ε is emissivity, σ is Stefan-Boltzmann constant. ρ_a is the atmospheric density, c_p is the atmospheric heat capacity, C_H is the heat transfer coefficient, L_v is the latent heat of vaporization, C_v is the moisture transfer coefficient and U is the wind speed in the boundary layer. $T_s - T_a$ is the temperature difference

and $Q_s - Q_a$ is the specific humidity difference between surface and atmospheric boundary layer at certain height.

Ice bottom energy balance

The oceanic heat flux F_w couples the thermodynamics of sea ice and ocean. It acts as the lower boundary condition to sea ice heat conduction equation. The oceanic heat flux can be calculated using the bulk formula (*Vancoppenolle et al.*, 2009)

$$F_w = \rho_w c_w C_h u_0^* \left(T_f - T_w\right), \tag{2.15}$$

where ρ_w is the density of sea water, c_w is the specific heat capacity of sea water, C_h is a heat transfer coefficient and u_0^* is the friction velocity. The temperature at the ice bottom is assumed to be at the freezing point T_f, which is a function of water salinity and pressure.

The heat balance at the ice bottom governs the ice thickness changes (*Petrich and Eicken*, 2016, p. 32)

$$\rho_i L_{si} \frac{dh_i}{dt} = F_c - F_w, \tag{2.16}$$

where ρ_i is the density of ice and L_{si} is the specific latent heat of fusion of ice. The term $\frac{dh_i}{dt}$ is the ice growth or melt rate. Imbalance in the fluxes at ice bottom results in release or uptake of latent heat. As latent heat is released the ice thickness increases as new congelation ice is formed at the ice bottom. The oceanic heat flux is usually positive and the thickness growth is limited by the conduction of heat through the ice.

The melting of sea ice is not limited only to the sea ice–ocean interface. Ice can melt at the top surface when the ice surface is at the freezing point and the heat flux is directed towards the ice. Sea ice can additionally experience lateral and internal melting. Lateral melting is a function of floe sizes. Internal melting is caused by brine interactions and absorption of shortwave radiation inside the ice.

Snow ice

Thermodynamic ice growth can be divided to congelation ice growth at the ice–ocean interface, and snow ice and superimposed ice growth on the ice–snow interface. Snow ice is formed when sea water floods over the ice and the slush freezes. Flooding occurs when snow is accumulated on the ice and the ice top is pushed below sea level. The equation for thickness growth of snow ice, derived from Archimedes' principle, is

$$\Delta h_{si} = \frac{\rho_s h_s - h_i \left(\rho_w - \rho_i\right)}{\rho_s + \rho_w - \rho_i}, \tag{2.17}$$

where ρ_s is the snow density, ρ_w is the density of sea water and h_s is the snow thickness. In a similar fashion superimposed ice can be formed from precipitated water or by refreezing melted snow on the snow–sea ice interface.

2.1.5 Salinity of sea ice

While most of the salt contained in sea water is rejected during the freezing process, some of it is trapped in sea ice. The salt is contained in brine pockets that are in thermodynamic equilibrium with the surrounding ice. Ice porosity structure changes in time with varying temperatures and brine salinity. Salinity of ice affects the thermodynamic properties, like heat and electric conductivity, heat capacity and latent heat of fusion of the sea ice are all heavily influenced.

The bulk salinity of newly formed ice S_i is given by the equation (*Petrich and Eicken*, 2016, p. 18)

$$\frac{S_i}{S_0} = \frac{\rho_w}{\rho_i}\phi_c \left(1 + \frac{h}{z_x}\right), \tag{2.18}$$

where S_0 is the salinity of the sea water and ϕ_c is a critical ice porosity limiting desalination and $\frac{h}{z_x}$ is the dimensionless thickness of the desalinating layer. The salinity of newly formed ice depends on the conditions during ice formation in a way that quickly growing ice has high salinity (*Petrich and Eicken*, 2016, p. 18).

As sea ice ages its salinity decreases through desalination processes, of which gravity drainage and meltwater flushing are the most important (*Notz and Worster*, 2009). Gravity drainage is driven by wintertime cooling from ice surface, which reduces the size of brine pockets and increases the salinity of the brine in the top layer. The density of brine increases with salinity and the brine density gradient in the sea ice becomes unstable. In porous ice the sea water is convected to the brine pockets, reducing the salinity of ice. Brine flushing is initiated by melt water accumulating on top of ice. The melt water percolates through the sea ice and flushes the brine, greatly reducing salinity of sea ice in summertime. Because of the various desalination processes, older ice is less saline than new ice and the salinity of sea ice is not vertically constant.

2.2 Oceanic and atmospheric drivers and indexes

Sea ice is a medium that is driven by forces of atmosphere and oceans, as shown in Section 2.1. Changes and variations in the forcing in many different scales are reflected in the sea ice conditions. The effects are not always straight forward, as there are various feedback effects in the sea ice–ocean–atmosphere system The mechanisms of atmospheric and ocean forcing on changing sea ice regime in the Arctic and Kara Sea are elaborated in this section.

2.2.1 Arctic warming and feedbacks

In 2001-2012 the mean annual surface temperature in the Arctic was over 1.5°C higher than in 1971-2000 (*Overland et al.*, 2014). The temperatures rose in all seasons with the warming greatest was in the cold season. Compared to mid-latitudes the increase is more than double. The phenomenon is known as Arctic amplification (*Screen and Simmonds*, 2010; *Serreze et al.*, 2009). The accelerated increase in tem-

perature in the Arctic regions is due to complex positive feedbacks related to changes in albedo, heat storage, longwave radiation fluxes and ice dynamics. The feedback effects have large seasonal variability, which also makes estimating the combined effect of feedbacks more complicated.

Melting of sea ice and the snow on top of it lower the surface albedo through formation of melt ponds, open water and thinning of ice. The albedo is also lowered by even small amounts of black carbon deposited on the surface (*Meier et al.*, 2011). Low albedo allows greater absorption of radiation and more melting creating a positive ice–albedo feedback.

The onset date of melting is becoming earlier in the year and more ice melts during the melting period (*Barber et al.*, 2017, p. 107). The ice free season becomes longer and more heat is accumulated in the ocean. The heat exchange between ocean and atmosphere becomes stronger in areas previously covered by ice. The lower atmosphere is warmed and is given more water vapor by the exposed ocean.

A secondary feedback comes from change in downward longwave radiation fluxes. As the sea remains ice free for longer periods and rising temperature increases evaporation, the lower atmosphere has more precipitable water. The water vapor and clouds are sources of downward longwave radiation fluxes. The increased amount of precipitable water in the atmosphere increases the longwave radiation flux to the surface. On the other hand, increased cloudiness could block shortwave radiation from reaching the surface and introduce a surface cooling, negative feedback. An increase in both the amount of precipitable water in the atmosphere and in the downward longwave radiation flux has been observed in the Arctic (*Ghatak and Miller*, 2013). Increase in ocean surface temperature causes a negative upward longwave radiation flux feedback (*Vihma*, 2014). The mixing of heat in the atmospheric boundary layer is also a defining factor in Arctic warming (*Boé et al.*, 2009). In a stable and shallow boundary layer, common in the Arctic, heat released by

the ocean is trapped close to surface increasing the warming effect. This feedback is diminishing as increased heating deepens the boundary layer (*Bintanja et al.*, 2012).

Ice drift speed and strain rate in the Arctic have significantly increased (*Barber et al.*, 2017, p. 117). The leading driver of the change has been suggested to be the thinning of sea ice. The mechanical strength of the thinner ice is lower, which allows faster ice drift and increased deformation. Faster transport of ice away from the Arctic reduces the time available for ice to grow and assists overall thinning. As ice strength decreases more leads are opened in the ice cover enhancing surface heat fluxes. In melting season the decreased albedo from lead opening allows for more heat accumulation in the ocean. The thinner ice is preconditioning higher melt rate and lower ice extent in the following summer. The ice thinning and increased heat accumulation from increased deformation complete another positive feedback loop.

The warming of the Arctic is expected to continue due to increasing atmospheric greenhouse gas concentrations (*IPCC*, 2014, p. 56). The dependency of future Arctic sea ice extent on the amount of greenhouse gases emitted to the atmosphere is highlighted by *Overland et al.* (2014). The changes could be mitigated in the scenario, where emissions of greenhouse gases are reduced but it is very likely that major changes will continue over the next decades.

2.2.2 The atmospheric and ocean circulation in the Kara Sea

The large scale atmospheric circulation patterns at high latitudes of Northern Hemisphere is characterized by westerly circulation, which is disturbed by easterly and meridional flow (*Volkov et al.*, 2002, p. 54). The prevailing wind directions in the Kara Sea region result from cyclonic activity and larger blocking pressure cells acting in the area. The wind forcing has considerable seasonal variability due to seasonal air pressure anomalies over the region. In the winter a stable high pressure cell over

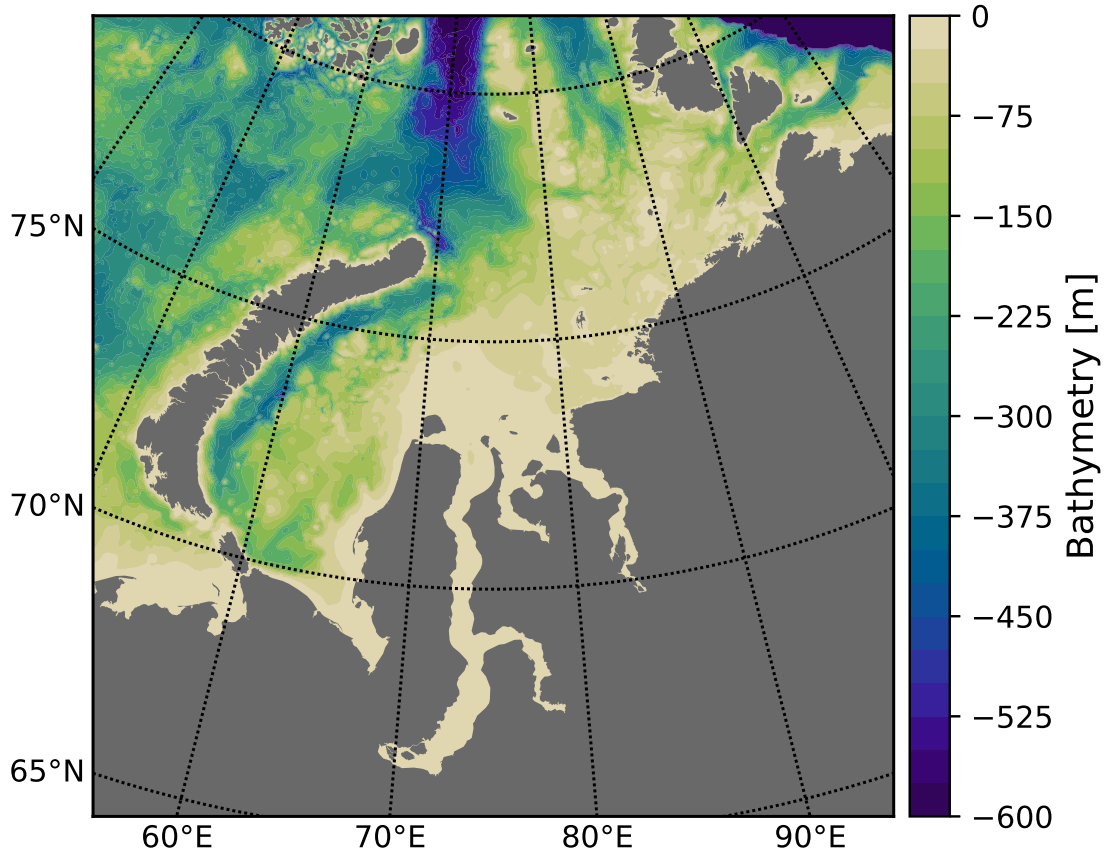

Figure 2.1: Bathymetry of the Kara Sea.

Siberia and low pressure cell over the Barents and Norwegian Seas surround the Kara Sea. In the summertime the Siberian high pressure cell is weaker and another high pressure cell develops over the Arctic Ocean (*Harms and Karcher*, 1999). A high pressure cell over the Kara Sea can block the cyclones from entering the area and induce easterly flow. Since cyclones tend to bring with them warm air from the Atlantic (*Boisvert et al.*, 2016), the winters when the high pressure cell is stable over the Kara Sea are generally colder and more favorable to production of ice (*Divine et al.*, 2005). Changes in the large scale atmospheric pressure systems and storm track can greatly change the climate. Increased atmospheric heat advection to the Barents and Kara Seas by cyclones is one potential reason for the decline of sea ice in the region *Jung et al.* (2017).

The general ocean circulation is characterized by eastward flow of water through the Kara Sea. Water from the Barents Sea enters the Kara Sea through the Kara Gate strait in the southeast and the opening between Novaya Zemlya and Franz Josef Land further north. *Panteleev et al.* (2007) estimated the mean climatological inflow to the Kara Sea to be 0.63 Sv[1] through Kara Gate and 1.18 Sv between Novaya Zemlya and Franz Josef Land. The major outflow regions are the Vilkitsky Strait south of Severnaya Zemlya and the St. Anna Trough and Voronin Trough in the north. In the deepest water layers the transport of water is mostly limited to these troughs. The outflow through the St. Anna Trough was estimated 1.17 Sv and the combined outflow through Vilkistky and Shokalsky Straits was 0.52 Sv.

The ice conditions especially in the northern Kara Sea are heavily affected by the transport of heat in ocean waters from the Barents Sea. Driven by the ocean heat transport, sea ice extent has been in fast decline in the region north of Novaya Zemlya, where the Barents Sea and the Kara Sea meet (e.g. *Onarheim and Årthun*, 2017). The great decline in sea ice area in this region can be explained by increased ocean heat transport and the atlantification of the Barents Sea (*Årthun et al.*, 2012).

A lot of the heat contained in the ocean waters entering the Kara Sea is in the layer of warm Atlantic water. The Arctic waters are commonly heavily stratified and the warm Atlantic water deeper in the ocean has been considered to have minimal effect on the surface heat budget. The stratification is, however, weakening and the Atlantic water is more easily mixed with the overlaying water layers. The increase in mixing releases more oceanic heat to the surface layer, which leads to increased melting of sea ice (*Polyakov et al.*, 2017).

The circulation in the Kara Sea is also influenced by the fresh water inflow from the rivers especially in the central Kara Sea (*Panteleev et al.*, 2007). The inflow volume of freshwater has great seasonal variability related to snow melt in

[1] Sv = $10^6 m^3/s$

the catchment areas and the spread of freshwater depends on the prevailing wind regime. The freshness of the sea water influences the thermodynamics of the sea through changes in stratification.

2.2.3 Effects of large scale atmospheric oscillations on the sea ice

Variations in large scale atmospheric pressure fields affect the circulation patters in the Arctic. The strength and phase of the oscillations are represented by various indexes including Arctic Oscillation (AO), North Atlantic Oscillation (NAO) and Arctic Dipole Anomaly (DA). Multidecadal variability in Arctic sea ice have been discovered by *Miles et al.* (2014) and in fast ice extent and thickness by *Polyakov et al.* (2003). The oscillations change the direction and strength of wind forcing with a significant impact on sea ice and water transport in oceans. By altering heat transport patterns, they can play a significant role in the decline of Arctic sea ice.

The Arctic Oscillation and the North Atlantic Oscillation

The Arctic Oscillation (AO) is defined by *Thompson and Wallace* (1998) as the leading principal component of sea level pressure anomaly in the Northern Hemisphere latitudes above 20°N from empirical orthogonal function method. The North Atlantic Oscillation (NAO) index is defined by *Rogers and Van Loon* (1979) as the oscillation in the normalized sea level pressure difference between the Azores high and Icelandic low. The NAO is often referred to as the North Atlantic's regional representation of the AO (*Parkinson and Cavalieri*, 2008).

The positive AO/NAO phase enhances the westerly winds and cyclonic component of the circulation in the Arctic. The positive phase is associated with enhanced ice transport away from the Siberian coast and out of the Arctic by the Transpolar Drift Stream. The divergence of ice from the Siberian coasts promotes lead forma-

tion leading to ice thinning (*Rigor et al.*, 2002). In the Kara Sea highly positive NAO in 1988-1996 promoted sustained flow of sea ice northward to the Arctic Ocean (*Kwok*, 2000).

During the negative phase large-scale cyclonic circulation is suppressed and ice motion has an anti-cyclonic anomaly. The anti-cyclonic Beaufort Gyre is stronger and the ice export by Transpolar Drift Stream becomes weaker as it turns more towards Canada. Ice is transported more from western to eastern Arctic, where convergence leads to thickness growth through deformations. Ice remains longer in the Canadian Basin and the overall ice thickness in the Arctic tends to increase (*Stroeve et al.*, 2011). However, *Chen et al.* (2016) found that a negative phase of AO is associated with reduced sea ice extent in the Barents and Kara seas. The effects of the AO could be changing due to changes in the sea ice cover, and ice volume may decrease despite oscillation phase being favorable to ice survival (*Stroeve et al.*, 2011).

The variations in large-scale air pressure fields and wind regime can significantly alter the ocean circulation pattern in the Kara Sea. The heat and salinity is advected to different regions, having effects on stratification and local near-surface water temperatures (*Panteleev et al.*, 2007).

The Arctic Dipole Anomaly

Another index used to explain the anomalous ice transports in the Arctic is the Arctic Dipole Anomaly (DA). It was first suggested by *Wu et al.* (2006) as the second empirical orthogonal function mode of sea level pressure anomaly in latitudes north of 70°N. DA has two centers of action located in the Arctic and the resulting drift anomaly is meridional. During the positive phase, DA has negative sea level pressure anomalies over Kara and Laptev Seas while a positive anomaly is present over the Canadian Archipelago and Greenland. During the negative phase, the sea

level pressure anomalies over the Arctic are the opposite to those in the positive phase and the negative anomaly is located over Northern Europe (*Wu et al.*, 2006).

The meridional drift anomaly resulting from DA allows great anomalous ice transports out of the Arctic during the positive phase. *Watanabe et al.* (2006) showed that DA has an important role in governing the export of sea ice out of the Arctic with the positive phase promoting and the negative phase restricting sea ice export. *Wang et al.* (2009) linked many Arctic record ice extent lows to an anomalous oceanic heat flux into the Arctic Ocean caused by the DA.

3. Data and methods

The analysis in this study uses data from NEMO-LIM3.6 coupled sea ice–ocean model and from satellite observation based sea ice concentration products, introduced in Sections 3.1 and 3.2 respectively. The methods used in data processing are presented in Section 3.3.

3.1 NEMO-LIM3

Hindcast simulation data from a coupled sea ice–ocean model is used to estimate the development of the sea ice conditions in the Kara Sea. As a part of model validation, the results from the model are compared with the observations. The NEMO-LIM3 model run was conducted at Finnish Meteorological Institute by Iiro Kokkonen, using a model setup developed by Andrea Gierisch and Robinson Hordoir. Data for boundary conditions and atmospheric forcing were provided by Petteri Uotila.

The coupled model consists of the Louvain-la-Neuve sea ice model version 3.6 (LIM3.6) (*Vancoppenolle et al.*, 2009; *Rousset et al.*, 2015) integrated in the Nucleus for European Modeling of the Ocean (NEMO) framework version 3.6. The whole model setup is referred to as NEMO-LIM3 in this thesis.

The simulation was carried out from June 1996 to December 2015 with daily output. The model domain includes the Kara Sea, a part of the Barents Sea and the White Sea. The scope of the study is limited only to the Kara Sea and the parts outside of it are masked as shown in Figure 3.1.

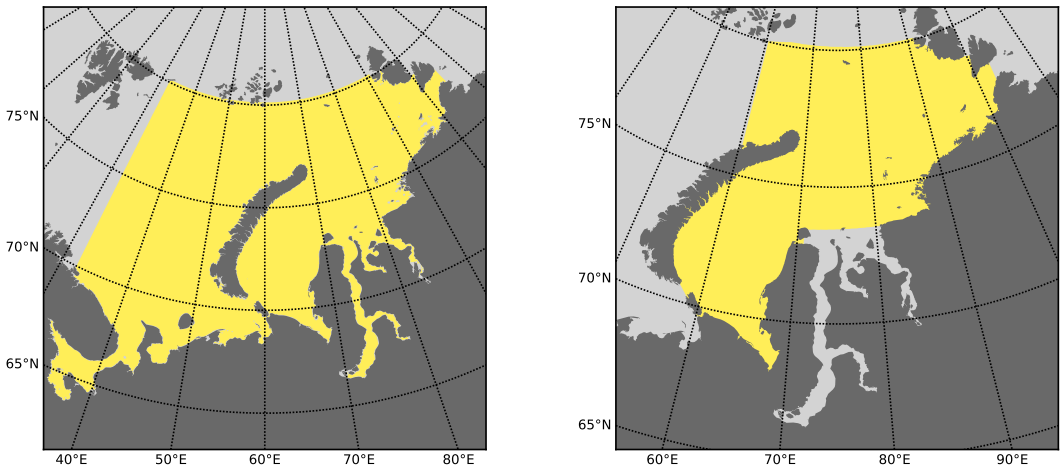

(a) NEMO-LIM3 model domain. **(b)** The Kara Sea study area.

Figure 3.1: **(a)** The model domain extending to the Barents Sea and **(b)** the study area limited to the Kara Sea with the estuaries of Ob and Yenisei excluded.

The model setup uses etopo1 bathymetry data (*Amante and Eakins*, 2009). The model grid resolution is 2 nautical miles. The number of vertical levels in the ocean model is 45 with 4 meters resolution at the surface. The ice model uses 5 thickness categories. The time step is 6 minutes. DRAKKAR 5.2 is used as atmospheric forcing (*Dussin et al.*, 2016), however, surface pressure data is taken from ECMWF ERA-Interim reanalysis dataset (*Dee et al.*, 2011). The boundary conditions for the setup are from a global eORCA025 (*Barnier et al.*, 2006) ocean/sea-ice model run carried out at Finnish Meteorological Institute. The boundary conditions include sea surface height, water temperature, salinity, barotropic currents as well as sea ice conditions. The ocean model boundary conditions include 9 tidal components from OTPS model (*Egbert and Erofeeva*, 2002). The runoff from rivers is included and uses the climatological data from eORCA025.

The ice model LIM3 uses multiple ice thickness categories for representation of the thickness distribution on sub-grid level. The dynamics and halo-thermodynamics of the sea ice are governed by the ocean model and atmospheric forcing. The sea ice

model uses elastic-viscous-plastic (EVP) rheology. The EVP rheology is modified from the *Hibler III* (1979) viscous-plastic rheology by adding an elastic term (*Hunke and Dukowicz*, 1997), which makes the rheology more computationally effective.

Fast ice in the model setup is parametrized. In areas with shallow water (depth < 15 m) the ice is assumed to be held stationary by grounded ridges. The ice model is not capable of forming fast ice by arching because of the limitations in the modeling of the internal mechanics of the ice pack (*Olason*, 2016).

The shortcomings in forcing data are a source of uncertainty in the model. The atmospheric heat fluxes in the sea ice–ocean model from the atmospheric forcing are dependent on the surface conditions in the reanalysis data. Sea ice observations are integrated into the reanalysis data and are indirectly fed into the sea ice–ocean model. For example ice cover in the reanalysis data allows a high temperature gradient between ocean and near-surface atmosphere. If the sea ice–ocean model has no ice cover, the high temperature gradient causes great heat loss from the ocean and promotes ice formation. The sea ice–ocean model is thus constrained by sea ice observational data and is not completely independent of the sea ice concentration observations used for validation.

The DRAKKAR 5.2 atmospheric forcing dataset used in our simulation is based on ERA-Interim reanalysis. The ERA-Interim atmospheric reanalysis has some known biases, but there has been attempts to correct them in DRAKKAR 5.2 forcing dataset (*Dussin et al.*, 2016). The climatological river run-off lacks the interannual variability and lowers the accuracy of modeled freshwater storage and stratification.

3.2 Satellite observation datasets

Two satellite observation based sea ice concentration datasets are used in this study: OSI-409 (*EUMETSAT Ocean and Sea Ice Satellite Application Facility*, 2015) and

OSI-450 (*EUMETSAT Ocean and Sea Ice Satellite Application Facility*, 2017). The OSI-409 ice concentration data is available from October 1978 to April 2015 in EASE grid with 12.5 km resolution. The OSI-450 data from January 1979 to December 2015 in EASE2 grid with 25 km resolution is used.

Both observational datasets are derived from multiple passive microwave satellite instruments. The OSI-409 data is from SMMR (1978–1987), SSM/I (1987–2013), and SSMIS (2013–2015) sensors. OSI-450 input data is from SMMR (1978–1987), SSM/I (1987–2008), and SSMIS (2006–2015). The ECMWF ERA-Interim atmospheric reanalysis data (*Dee et al.*, 2011) has also been utilized in the products for atmospheric correction of the brightness temperature.

The observational data is available every second day during the SMMR period (1978–1987). Daily data is available since August 1987. Notable gaps present in the observational datasets due to lack of satellite data include the periods 29/3–23/6 1986 and 03/12/1987–12/1/1988. All missing gaps in satellite data are listed in the respective dataset product user manuals (*Eastwood et al.*, 2017; *Sørensen et al.*, 2017).

Both datasets use a hybrid ice concentration algorithm (*Tonboe et al.*, 2016). The hybrid ice concentration algorithm combines the Bootstrap frequency mode algorithm (*Comiso*, 1986) and the Bristol algorithm (*Smith*, 1996). The Bootstrap algorithm is used over open water, because it has low sensitivity to atmospheric noise at low ice concentrations. The Bristol algorithm is used over ice in the hybrid algorithm. It has low sensitivity to variability in ice surface emissivity and to atmospheric emissivity, especially at high ice concentrations. Weighting functions of the algorithms in the two datasets are different. Inconsistencies between sensors have been minimized by using dynamical tie-points. Compared to OSI-409, OSI-450 has improved algorithms and processing chain. Most noticeably the open water filter

has been improved from OSI-409 to OSI-450 resulting in less falsely detected sea ice in open water areas (*Sørensen et al.*, 2017).

The two observational datasets, and passive microwave data in general, have some shortcomings according to *Sørensen et al.* (2017). Distinguishing melt ponds on ice from open water is difficult and the ice concentrations are underestimated in the melting season. Some thin ice may also be interpreted as ice of low concentration because of the similar signatures. Land spillover and effects of weather are corrected for in the algorithms. The correction may still leave false ice near coasts or falsely filter some sea ice. The footprints of the sensors do not match the grid resolution of the datasets and may induce a smearing effect in the gridded data. The interpolation of missing data causes some error but is necessary for example for calculating the total extent of sea ice.

3.3 Methods

Monthly means are calculated from the daily simulation and observational data. Months with too few observational data points are rejected from the analysis by introducing a limit requiring data from at least 10 days when calculating the monthly mean. Because of this criterion, observational data are missing from: April–June 1986, January 1987 and December 1987 in both OSI-409 and OSI-450 datasets and from June 1994 in OSI-409 dataset. Any short gaps in the data are interpolated. In spatial mean calculations the means are weighted by the grid cell areas.

The monthly mean ice concentrations between 1997–2015 are examined to detect seasonal and regional differences in mean ice conditions. Monthly mean ice concentration is calculated from the simulated period, 1997–2015, to make it possible to compare the simulated and observed results. Monthly mean fields of ice concentration are first calculated for each grid cell and month, and are then averaged for each of the twelve months of the year.

In this thesis the ice covered fraction (mean ice concentration of the sea) is used as a measure of the area of the sea ice cover. Our definition for the ice covered fraction is the total ice covered surface area divided by the total surface area of the sea. It is calculated as the grid cell area weighted average of the ice concentrations of all grid cells. Ice covered fraction, which is derived from ice area, was selected over ice extent as the measure of ice coverage because it is more reliable when comparing data with different grid resolutions (*Notz*, 2014). Ice extent (the total area of grid cells, where ice concentration is over 15%) is commonly used when dealing with ice concentration derived from satellite retrievals because it alleviates the uncertainties in the retrieved satellite data. The passive microwave signature is especially affected by weather interference and in the summertime by melt ponds on ice (*Notz*, 2014). When using ice covered fraction, as in the present study, these uncertainties are not avoided and may cause some error when estimating the summer ice coverage from the observational datasets.

Ice thickness is calculated from ice model data only. The mean ice thickness is calculated from the whole Kara Sea. Any grid cells where ice concentration is below 15% are counted as ice of zero thickness. This method is applied in order to reduce the effect of thick residual ice floes in low modeled concentration ice fields when calculating the mean ice thickness. The mean is weighted by respective grid cell areas but not by ice concentrations in the cells. By including the connection to ice concentration the mean ice thickness reported here is more closely associated with the total volume of the sea ice rather than the thickness of individual ice floes.

To detect trends in the data, linear regression lines are fitted to the calculated monthly mean ice covered fraction and simulated ice thickness data. Trend fitting in the analysis is done using the linear least squares method. The error of the fitted trends is estimated based on the standard error of the regression. The statistical significance of the trends is represented by the p-value. The p-value is obtained

from a hypothesis test, where the null hypothesis is no trend in the data. The p-value is the probability that the null hypothesis is true. Trends with p-values over a certain threshold, α, are rejected as not significant. In this thesis the value $\alpha = 0.05$, corresponding to 95% confidence level, is used when testing statistical significance.

For studying the interannual variations in the data the time series are detrended to reveal anomalies. The detrending is done by extracting the trend that was found using the linear least squares method from the original time series. The correlation of the detrended time series from simulation and observational datasets are studied. For the correlation analysis the Pearson's correlation coefficient is used.

The number of ice free days is calculated from the ice concentration data. In the gridded model and observational data, a cell is considered ice free if the ice concentration is lower than 15%. Gaps in the datasets are interpolated because full temporal coverage is necessary for the calculation. In case of missing data in the beginning or the end of the year, for annual ice free days the data is extrapolated to cover the rest of the year.

4. Results

In this section contains the results from the analysis based on the data and methods presented in Section 3. Maps of monthly average ice concentrations are calculated to examine subregional differences and seasonal cycle in the ice conditions. Trends and variability of sea ice covered fraction (mean sea ice concentration) in the Kara Sea are studied for each month separately. The Kara Sea is divided into four distinct sectors and the changes in ice covered fraction are studied in them. Simulated changes in mean sea ice thickness are also examined. An estimate of spatial distribution and changes in the annual ice free time is given. The results from the three datasets, OSI-450, OSI-409 and NEMO-LIM3, are compared when applicable.

The monthly mean maps and time series are obtained from each month separately and the results from only few selected months will be presented and analyzed in this thesis. The months chosen for closer examination are March, June, September and December. These months were selected on the basis that they would sufficiently represent the annual cycle since March and September are the months of maximum and minimum ice extent, respectively. June and December are half way between the months of maximum and minimum ice extent and are representative of ice conditions during the freezing and melting seasons.

4.1 Monthly mean ice concentration

The maps of 1997–2015 mean ice concentration in the Kara Sea in March, June, September and December are shown from all three datasets in Figures 4.1–4.4. The March mean ice concentration field is shown in Figure 4.1. The simulated ice concentration is 100% virtually everywhere while there is still a wide area of lower ice concentration north of Novaya Zemlya in the observational datasets. In June (Fig. 4.2) the ice cover begins to melt and the ice concentrations have a great range of spatial variance. The ice concentrations are the highest along the east coast of Novaya Zemlya and in the northeastern Kara Sea. These are the locations where ice pack accumulations often survive long into summer (*Volkov et al.*, 2002, pp. 232–235). The ice concentrations in the river estuaries remain high while according to (*Volkov et al.*, 2002, pp. 308–309) they are on average the first area to lose ice cover in the spring. The ice concentration is high in the estuaries in the model simulation because of the parameterized fast ice that still remains there in June. In September (Fig. 4.3) the Kara Sea is ice free with the exception of the northeastern parts. This means that in some years multi-year ice has been formed in the northern Kara Sea or it has been transported there from the Arctic Ocean. Some ice also remains in the river estuaries and bays, but they are likely falsely detected. By December (Fig. 4.4) a large part of the sea is again ice covered with ice concentration reaching 100% in all datasets in the eastern half of the sea. Areas of low ice concentration persist near Kara Gate and north of Novaya Zemlya in the observation based datasets. In the observed data, the river estuaries are not completely frozen either. Based on the ice model data, the ice concentration is significantly higher than observed in all the mentioned areas.

The truthfulness of observed ice concentration data in the relatively narrow estuaries of Ob and Yenisei is questionable. In winter time the river estuaries remain partially ice free while they are expected to be covered entirely by fast ice (*Volkov*

et al., 2002, pp. 346–347). In summer and autumn ice concentrations remain in the 20%–60% range, also suggesting bad data quality.

Observation based datasets have a relatively coarse resolution. Hence, the number of data points in the estuaries might not be sufficient for accurately estimating the ice concentration and derived quantities or for comparing the ice conditions between the different datasets. Due to these findings we decide not to include the data from the estuaries in further analyses.

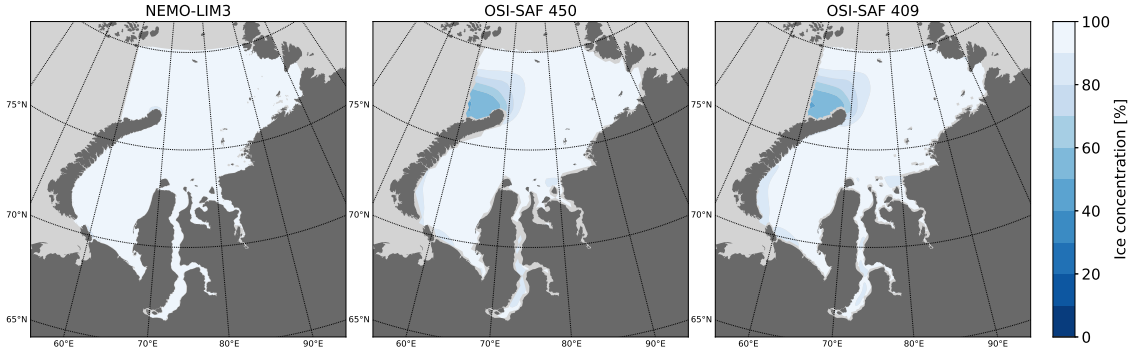

Figure 4.1: Simulated and observed mean ice concentration; March 1997–2015.

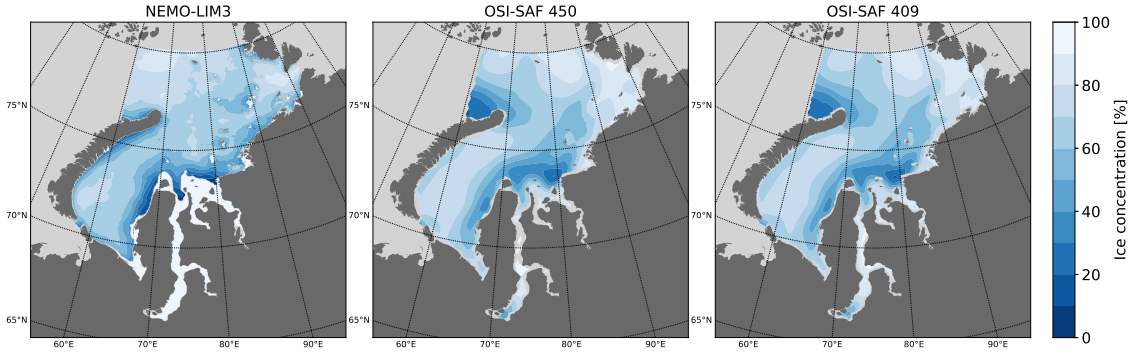

Figure 4.2: Simulated and observed mean ice concentration; June 1997–2015.

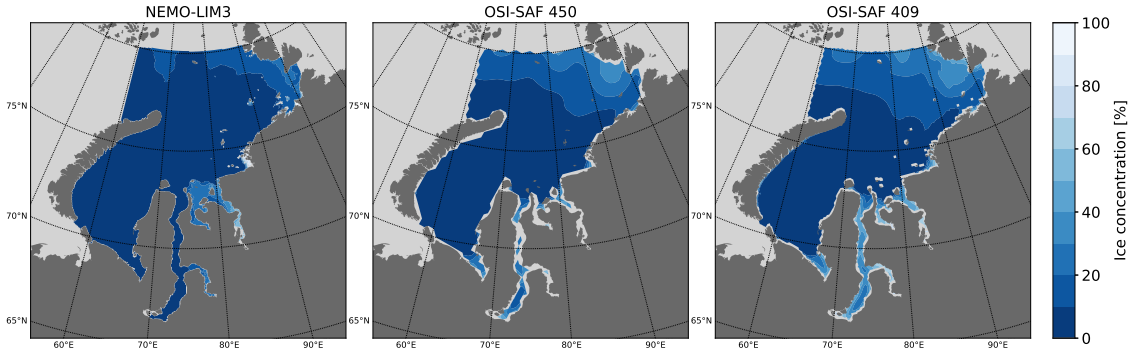

Figure 4.3: Simulated and observed mean ice concentration; September 1997–2015.

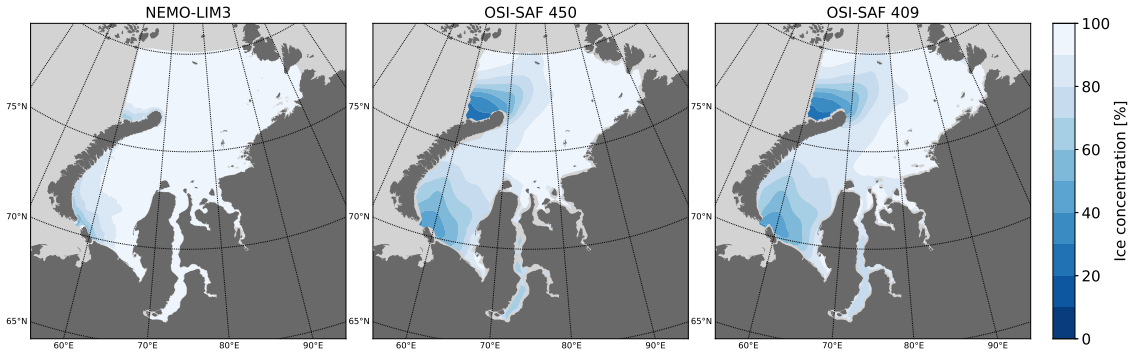

Figure 4.4: Simulated and observed mean ice concentration; December 1997–2015.

4.2 Ice covered fraction trends and variability

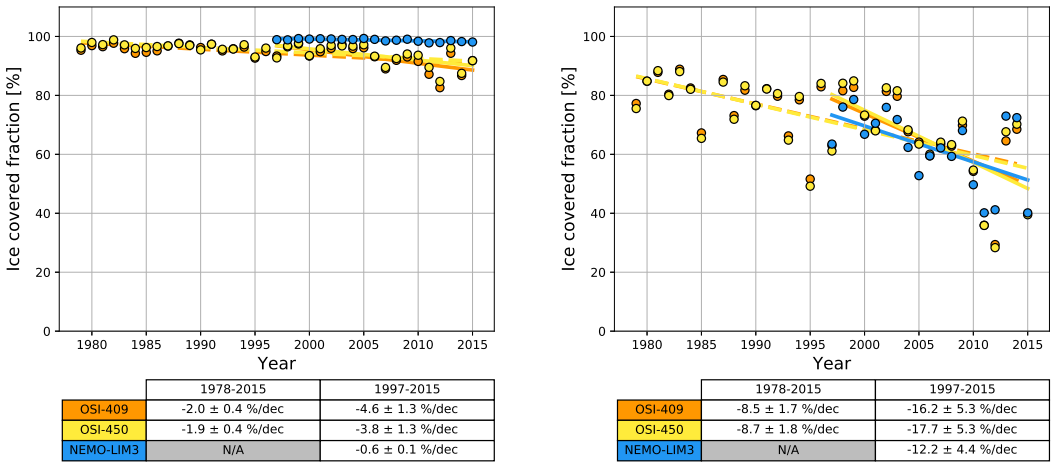

(a) March.

(b) June.

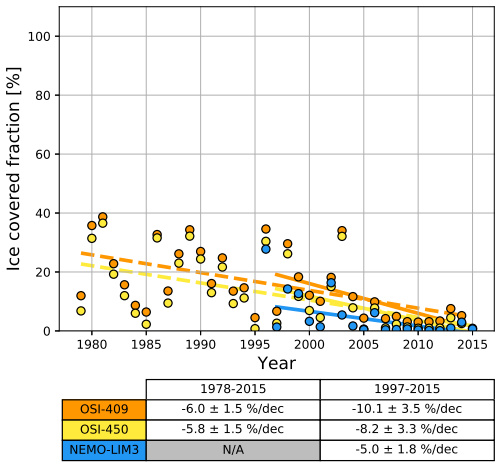

(c) September.

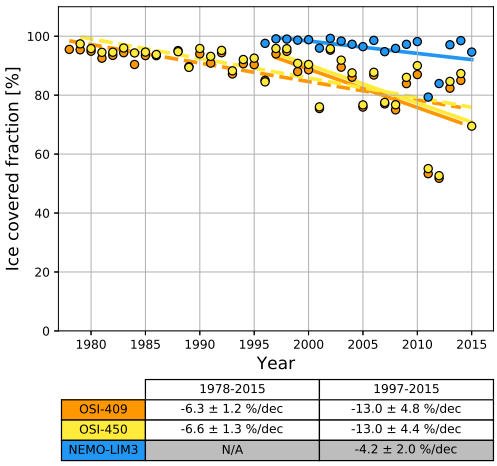

(d) December.

Figure 4.5: Time series (dots) and trends (lines) of monthly mean ice covered fraction in March **(a)**, June **(b)**, September **(c)** and December **(d)** calculated from the whole Kara Sea for the datasets OSI-409 (orange), OSI-450 (yellow), and NEMO-LIM3 model (blue).

The monthly mean ice covered fractions in the Kara Sea, excluding the estuaries, are shown in Figure 4.5. In the figure the mean ice covered fraction of individual

years is represented by dots. The fitted linear regression trends are represented by dashed lines between 1978–2015 and solid lines between 1997–2015.

The tables show the linear trends (± the standard error of the estimated slope). The background color of the table cells indicates the statistical significance of the trend. The trends in white cells are statistically significant with p-value below 0.05, while the trends in gray cells are not statistically significant at 95% confidence level.

Figure 4.5 shows that there is a declining trend present in all months both in long term since 1978 and in short term since 1997.

In March (Fig. 4.5a) the observed trends in 1978–2015 are about -2%/decade. The short term change between 1997–2015 is about twice as high. The ice model has a very small negative trend.

In June the ice covered fraction (Fig. 4.5b) exhibits a fast decline. The trends are from -8% to -9% per decade in long term, accelerating to -16% to -18% per decade in short term. The trend and variations from ice model decently match those from the satellite observation derived datasets.

The September trends (Fig. 4.5c) have also accelerated from -6% per decade in long term to -10% and -8% per decade in short term. The ice model has underestimated the ice covered fraction slightly, especially before 2005. The variability has diminished as the mean ice covered fractions have fallen closer to zero percent.

December ice covered fractions (Fig. 4.5d) are also acceleratingly declining. The declining trend in observational datasets has doubled from about -6%/decade in 1978-2015 to -13%/decade in 1997-2015. The ice model has a smaller, not statistically significant, trend.

The ice model has consistently overestimated the ice covered fraction in wintertime and underestimated it in summertime. The ice model generally tends to underestimate the decline of the ice cover. The variability appears to increase in

months that have been almost entirely ice covered and decrease in months that have had low ice covered fraction.

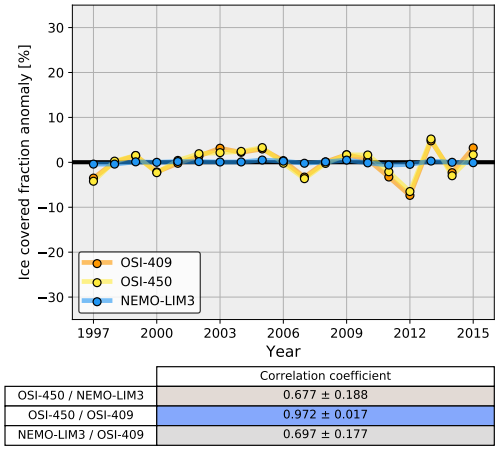

	Correlation coefficient
OSI-450 / NEMO-LIM3	0.677 ± 0.188
OSI-450 / OSI-409	0.972 ± 0.017
NEMO-LIM3 / OSI-409	0.697 ± 0.177

(a) March.

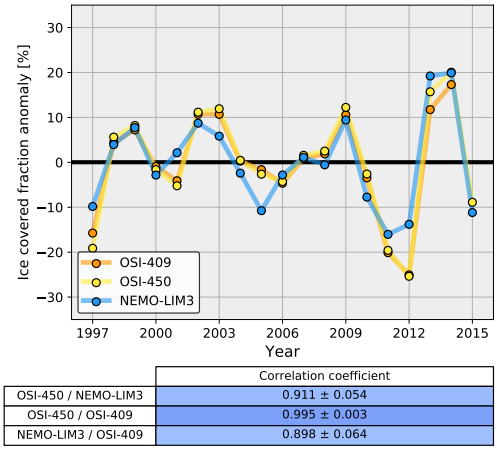

	Correlation coefficient
OSI-450 / NEMO-LIM3	0.911 ± 0.054
OSI-450 / OSI-409	0.995 ± 0.003
NEMO-LIM3 / OSI-409	0.898 ± 0.064

(b) June.

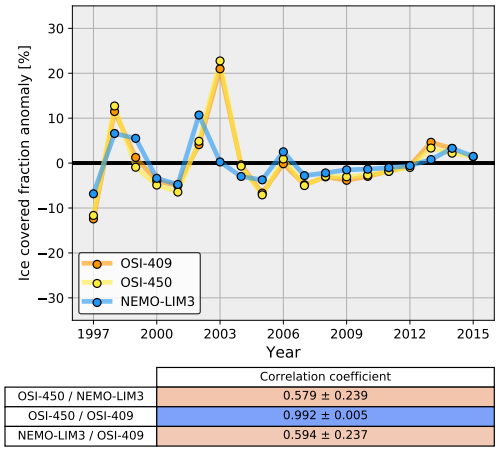

	Correlation coefficient
OSI-450 / NEMO-LIM3	0.579 ± 0.239
OSI-450 / OSI-409	0.992 ± 0.005
NEMO-LIM3 / OSI-409	0.594 ± 0.237

(c) September.

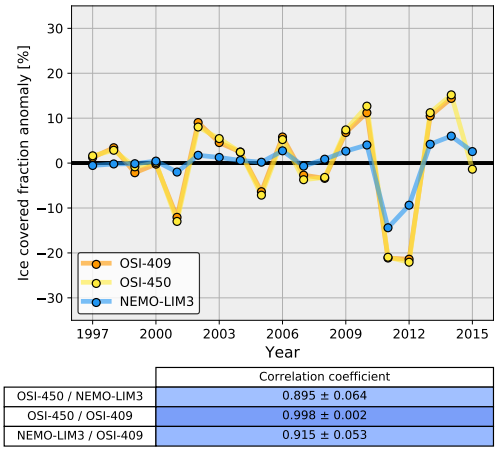

	Correlation coefficient
OSI-450 / NEMO-LIM3	0.895 ± 0.064
OSI-450 / OSI-409	0.998 ± 0.002
NEMO-LIM3 / OSI-409	0.915 ± 0.053

(d) December.

Figure 4.6: Detrended time series of monthly mean ice covered fraction for **(a)** March, **(b)** June, **(c)** September and **(d)** December for the period 1997–2015. The y-axis gives the anomaly in ice covered fraction in the Kara Sea. The tables show the correlation coefficients between the different time series ± 95% confidence interval.

To compare the interannual variations in different time series, the anomaly of ice covered fraction from the linear regression line is examined. Figure 4.6 shows comparison of the detrended time series from March (Fig. 4.6a), June (Fig. 4.6b),

September (Fig. 4.6c) and December (Fig. 4.6d). Assuming a steady linear trend in the ice covered fraction, the deviation from the linear regression is equal to anomaly from the expected ice covered fraction. A quick look at Figure 4.6 reveals that the anomalies in ice model data matches the anomalies in observational datasets quite well.

For the majority of months the anomalies are similar in all datasets and the respective correlations are high. The correlation coefficient of ice model and observational datasets is over 0.85 in January, February, May, June, July, October, November and December.

In early spring months (January–April) the deviations in the ice model data are small. The correlation between the detrended ice model and observation time series is lowest in March, April and September. When most of the sea is ice covered in March and April the year-to-year differences in the ice edge north of Novaya Zemlya and near Kara Gate can be the main source of deviations. The deviations in these regions are not accurately captured by the ice model and the resulting anomalies in the ice model data are smaller. In September the amount of ice remaining is minimal and local differences between the model and observations could cause low correlation. The anomalously high observed ice covered fraction in September 2003 could not be captured by the model.

There are some events causing anomalously high or low ice covered fraction whose strength is not captured well by the ice model. These include the exceptionally high ice covered fraction in July–September 2003, which is greatly underestimated by the ice model. The ice model, however, manages to capture many other similarly strong anomalies, for example in May–August 2014. Even though the ice model may overestimate or underestimate the ice covered fraction and trends, the similar anomalies in all datasets indicate that the responses to various atmospheric and oceanic forcing phenomena in the ice model are realistic.

4.3 Ice covered fraction in subregions

Examination of monthly mean ice covered fraction in different subregions can help explain the reasons behind the changes and inter-annual variability in the ice cover. Therefore, the sea is divided into four sectors since there are notable subregional differences in the monthly mean ice concentrations and their assumed main contributing drivers.

The division of the Kara Sea into sectors is shown in Figure 4.7. The sector N ("northern") exhibits notable differences in the mean ice concentrations between model and observational data. This is the area where the ice and water transport between the Barents Sea, the Kara Sea and the Arctic Ocean is a very significant defining factor for the ice conditions. Sector C ("central") is the sector where the direct impact of boundary fluxes is the lowest. It is also the sector where the differences in mean ice concentrations between the datasets are the smallest. Sector S ("southern") is geographically the southernmost of the four and its ice conditions are affected by transport through the Kara Gate strait. Sector F ("fast ice") is the sector with the largest fast ice formations during the winter (*Divine et al.*, 2003). The sector is also characterized by multiple small islands, shallow waters and inflow of fresh water from the large rivers.

The Figures 4.8–4.11 show the monthly mean ice covered fraction in each sector. The March mean ice covered fractions are shown in Figure 4.8. The model simulation shows nearly 100% ice coverage in all sectors throughout the time series. Sectors N and S show minimal but statistically significant negative trends. The trends in the other two sectors are negligible. The observational data in sectors C and F show an ice covered fraction of 90% to 100% in all years with small interannual variability. The ice model has slightly higher ice covered fraction with less interannual variability than the observed datasets in these sectors. In sector S there is a small decreasing trend apparent in all datasets. The changes have been most

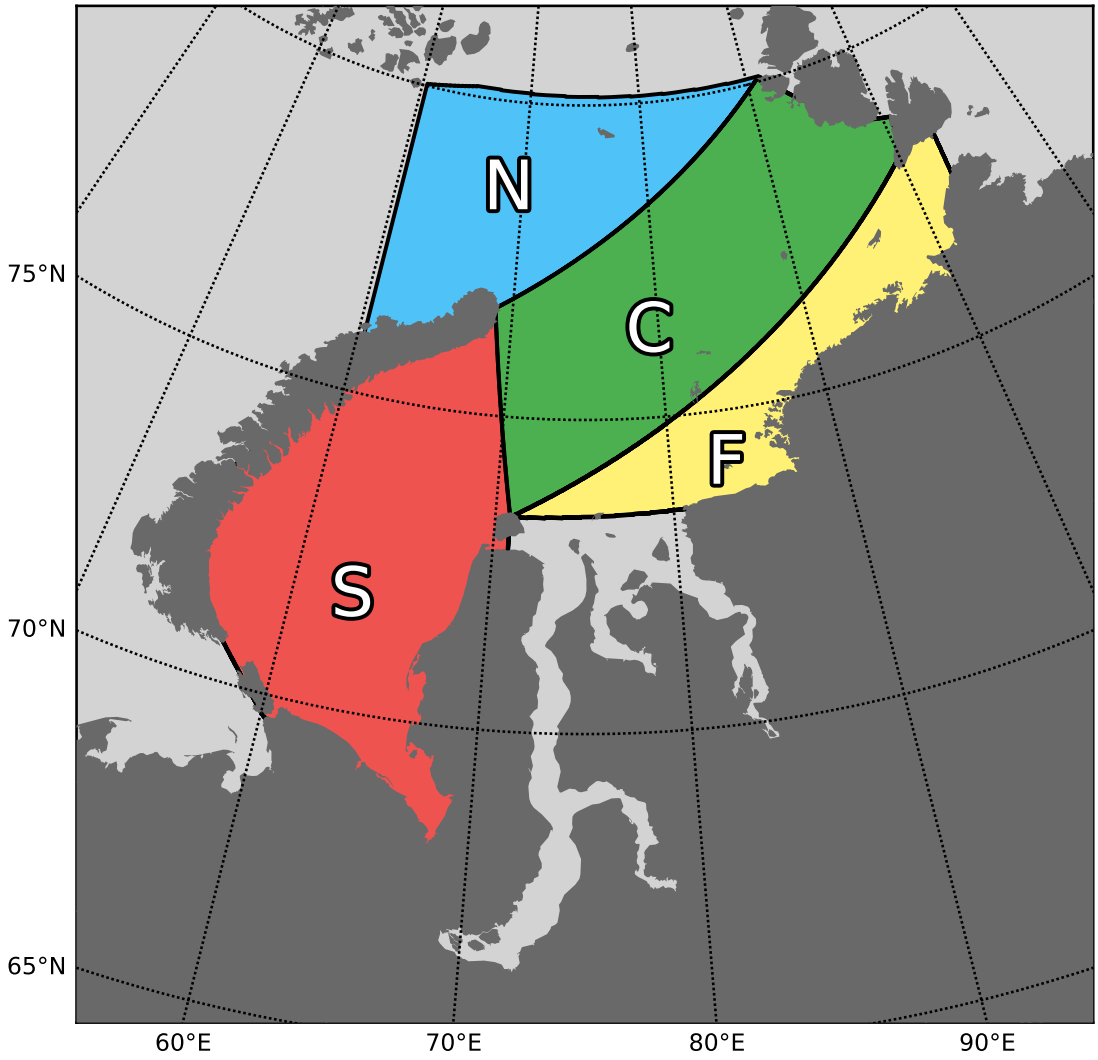

Figure 4.7: The Kara Sea divided into four sectors.

considerable in sector N. The decline accelerated from about -7%/decade in the long period (since 1978) to -13%/decade in the more recent period (since 1997) with all trends being statistically significant. The variability in mean ice covered fraction has greatly increased as close to full ice coverage is no longer reached. In sector N the trend from ice model data is weak (-0.8%/decade since 1997). In the other sectors the trend from ice model data is close to the trends from observational data, but the ice covered fractions are slightly overestimated.

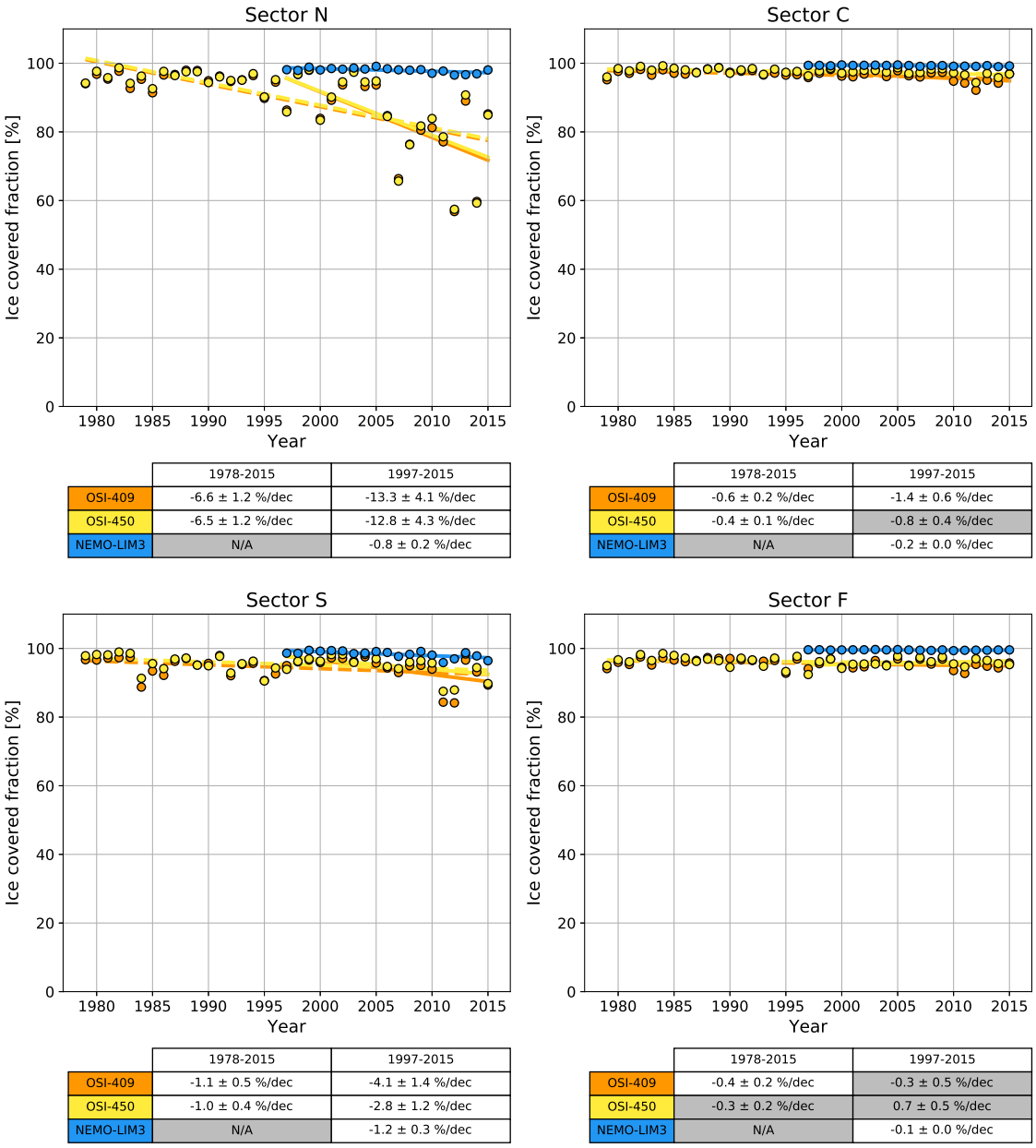

Figure 4.8: March mean ice covered fraction and the respective trends for 1978–2015 and 1997–2015 in the four sectors.

In the middle of the melting season in June (Fig. 4.9) the ice covered fractions show high negative trends in all sectors. The long term change is fastest in sector N where the trends since 1978 exceed 12% per decade. Based on the observational datasets the decline has accelerated in sectors N, S and F. The decline in ice covered

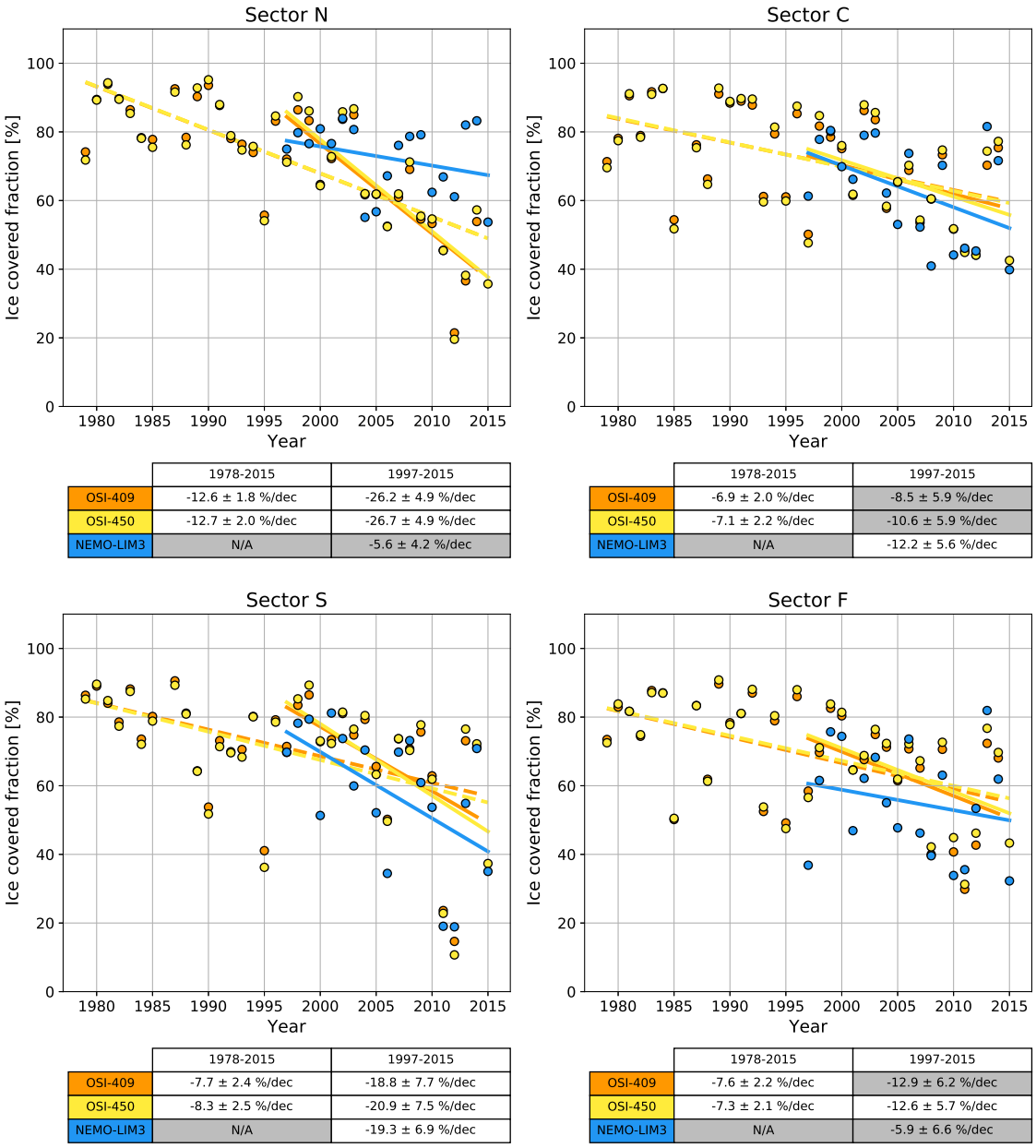

	1978-2015	1997-2015
OSI-409	-12.6 ± 1.8 %/dec	-26.2 ± 4.9 %/dec
OSI-450	-12.7 ± 2.0 %/dec	-26.7 ± 4.9 %/dec
NEMO-LIM3	N/A	-5.6 ± 4.2 %/dec

	1978-2015	1997-2015
OSI-409	-6.9 ± 2.0 %/dec	-8.5 ± 5.9 %/dec
OSI-450	-7.1 ± 2.2 %/dec	-10.6 ± 5.9 %/dec
NEMO-LIM3	N/A	-12.2 ± 5.6 %/dec

	1978-2015	1997-2015
OSI-409	-7.7 ± 2.4 %/dec	-18.8 ± 7.7 %/dec
OSI-450	-8.3 ± 2.5 %/dec	-20.9 ± 7.5 %/dec
NEMO-LIM3	N/A	-19.3 ± 6.9 %/dec

	1978-2015	1997-2015
OSI-409	-7.6 ± 2.2 %/dec	-12.9 ± 6.2 %/dec
OSI-450	-7.3 ± 2.1 %/dec	-12.6 ± 5.7 %/dec
NEMO-LIM3	N/A	-5.9 ± 6.6 %/dec

Figure 4.9: Same as Figure 4.8, but for June mean ice covered fraction.

fraction in sector N since 1997 is exceptionally fast, exceeding -26% per decade in the observational datasets. The interannual variability in June mean ice covered fractions is high and it dominates the time series. The trends from observational datasets since 1997 are not statistically significant in sectors C and F. In sectors C and S the ice model trends are very close to the observed trends. In sectors N and

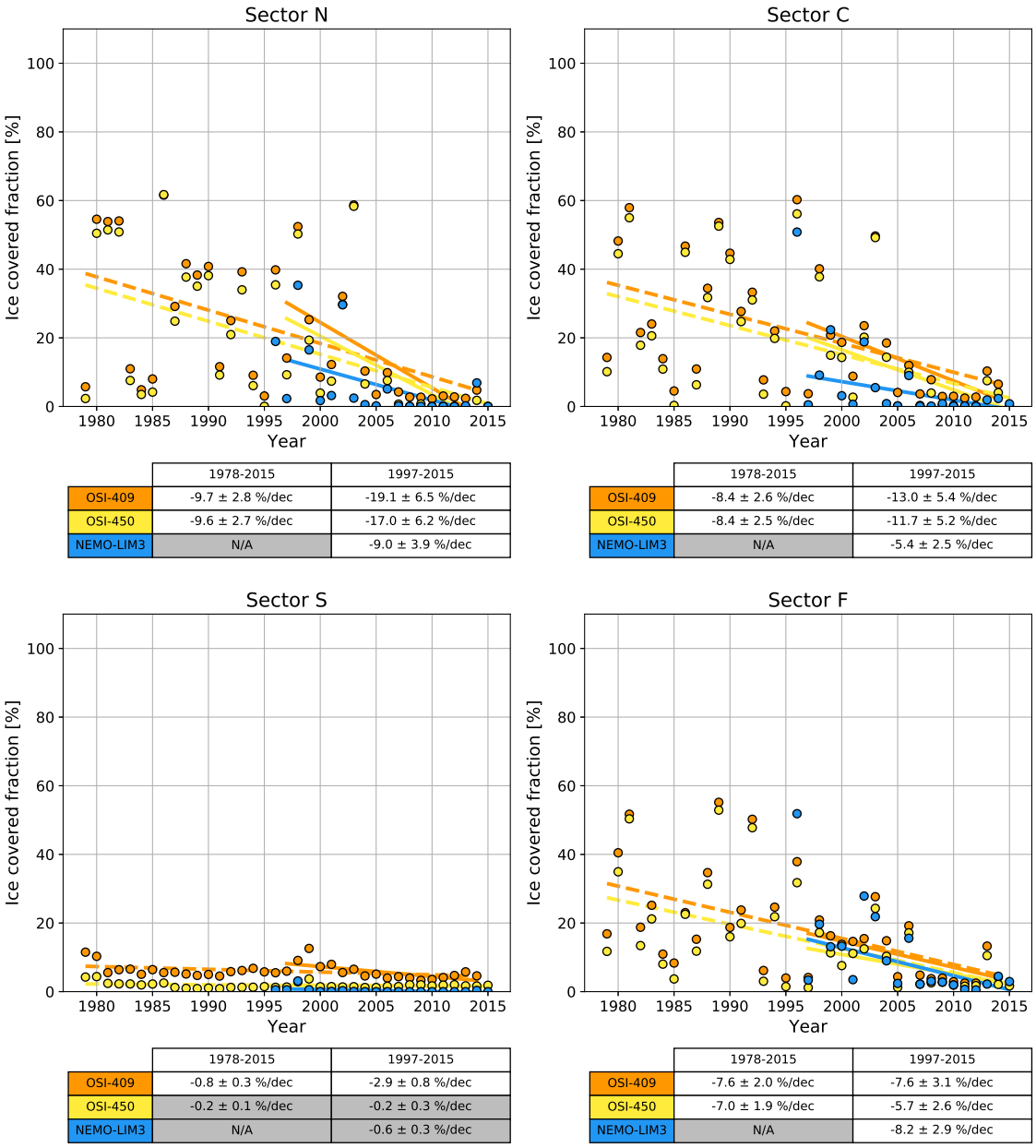

Figure 4.10: Same as Figure 4.8, but for September mean ice covered fraction.

F the ice model has small negative trends that are not statistically significant. The range of interannual variability in model data is similar to that in the observed data.

Figure 4.10 shows the mean ice covered fraction in the four sectors in September. There are significant negative trends in sectors N, C and F with the decline slightly accelerating in sectors N and C. In sector S the ice covered fraction has

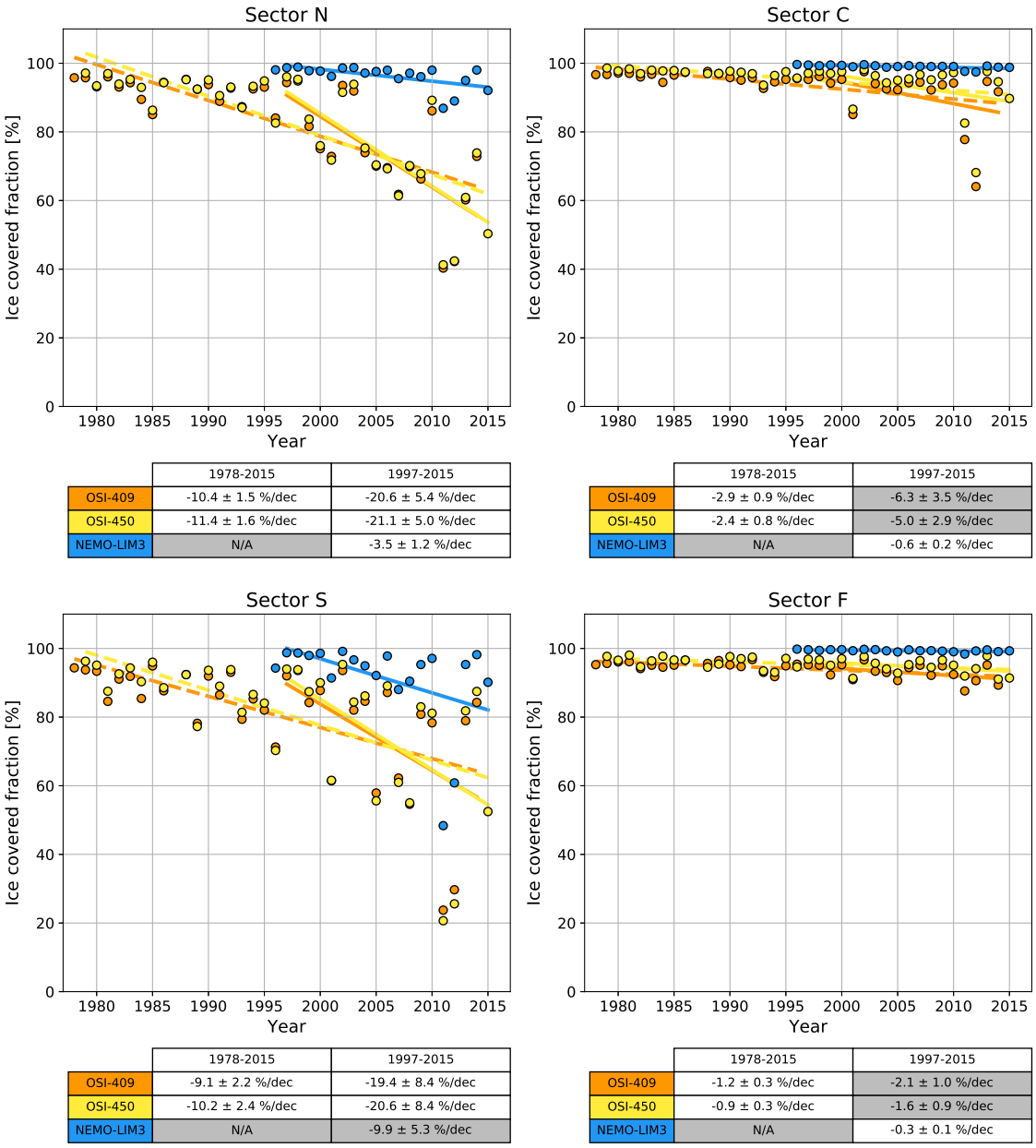

	1978-2015	1997-2015
OSI-409	-10.4 ± 1.5 %/dec	-20.6 ± 5.4 %/dec
OSI-450	-11.4 ± 1.6 %/dec	-21.1 ± 5.0 %/dec
NEMO-LIM3	N/A	-3.5 ± 1.2 %/dec

	1978-2015	1997-2015
OSI-409	-2.9 ± 0.9 %/dec	-6.3 ± 3.5 %/dec
OSI-450	-2.4 ± 0.8 %/dec	-5.0 ± 2.9 %/dec
NEMO-LIM3	N/A	-0.6 ± 0.2 %/dec

	1978-2015	1997-2015
OSI-409	-9.1 ± 2.2 %/dec	-19.4 ± 8.4 %/dec
OSI-450	-10.2 ± 2.4 %/dec	-20.6 ± 8.4 %/dec
NEMO-LIM3	N/A	-9.9 ± 5.3 %/dec

	1978-2015	1997-2015
OSI-409	-1.2 ± 0.3 %/dec	-2.1 ± 1.0 %/dec
OSI-450	-0.9 ± 0.3 %/dec	-1.6 ± 0.9 %/dec
NEMO-LIM3	N/A	-0.3 ± 0.1 %/dec

Figure 4.11: Same as Figure 4.8, but for December mean ice covered fraction..

remained close to zero for the whole period. With the exception of sector S the interannual variability has been substantial until 2005, but has since then diminished as the ice covered fraction fall closer to zero. Since 2005 the mean ice covered fraction has not exceeded 20% in any of the sectors. The ice model matches the

observational data in sectors F and S. In sectors N and C the modeled ice covered fractions and their trends are smaller than in the observational datasets.

The December ice covered fractions shown in Figure 4.11 are in clear decline in sectors N and S, while the trends are smaller in sectors C and F. The interannual variability in December has increased especially in sectors N and S. The ice model generally overestimates the ice covered fraction and has a lower variability. The anomalously mild winters in 2011 and 2012 are captured by the ice model but the magnitude of the anomaly is close to the observations only in sector S.

4.4 Ice thickness

Figure 4.12 shows time series for the selected months of the monthly mean ice thickness in the Kara Sea calculated from the ice model data. The ice thickness reported here is not equal to the mean ice floe thickness as it takes into account the open water areas as ice of zero thickness as explained in Section 3.3. The monthly mean ice thickness is decreasing in all months, including the months not shown here, with all trends being statistically significant at 95% confidence level. The trends are biggest in spring and early summer when the mean ice thickness is also highest. The mean ice thickness has decreased by 35 cm/decade in June and by 32 cm/decade in March. The minimum of March mean ice thickness in the early half of the time series, 1997 to 2005, was 97.1 cm in 2000. After 2005 the mean ice thickness has been higher than in 2000 only in 2010 and 2011. The December trend is smaller than the trends in May and June in absolute terms, but about as high relative to the mean ice thickness. The mean thickness and its trend are smallest in September. The mean ice thickness reaches values closer to 20 cm more frequently in the earlier half of the time series while in more recent years the mean ice thickness in March has remained close to zero. The interannual variability in the ice thickness is highest in the spring. The March mean ice thickness may vary by tens of centimeters from

one year to the next, while in the autumn the variability is naturally low because the mean thickness is close to zero.

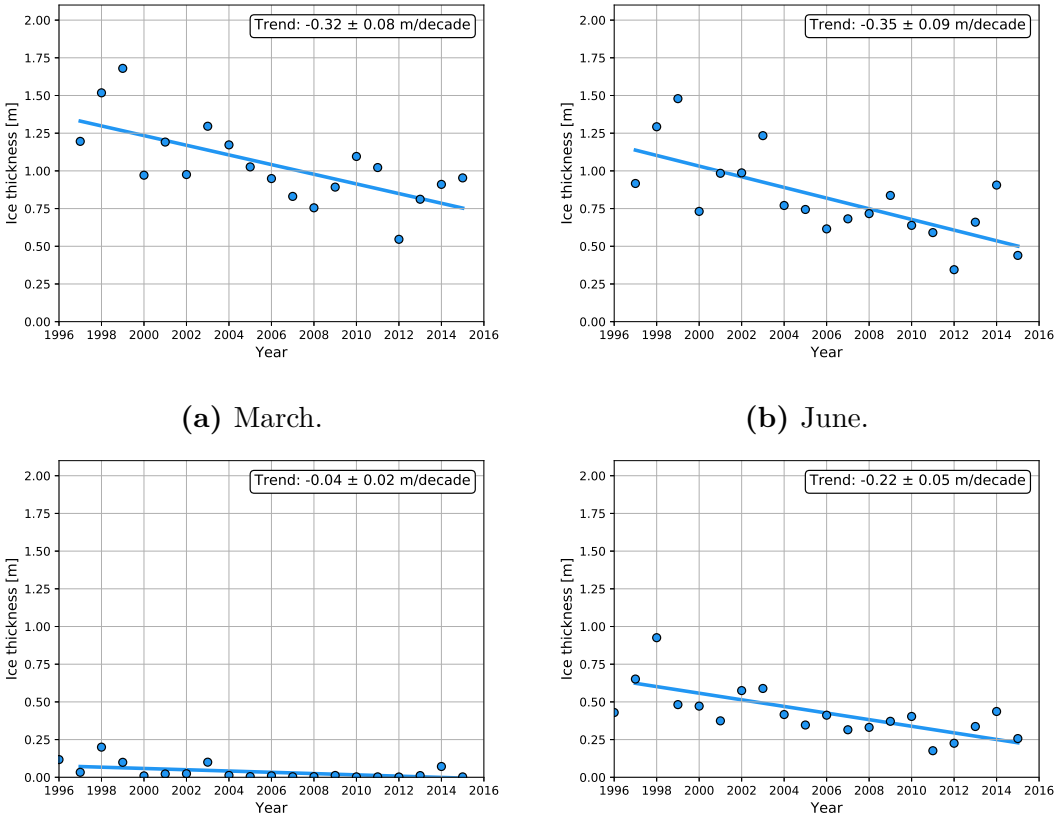

(a) March. **(b)** June.

(c) September. **(d)** December.

Figure 4.12: Simulated NEMO-LIM3 monthly mean ice thickness in the Kara Sea for **(a)** March, **(b)** June, **(c)** September and **(d)** December and the respective fitted trend lines for 1997–2015.

4.5 Ice free time

The annual distributions of the number of ice free days are shown from years 1990 (Fig. 4.13), 1998 (Fig. 4.14), 2003 (Fig. 4.15), 2006 (Fig. 4.16), 2012 (Fig. 4.17) and 2015 (Fig. 4.18). The years presented here were chosen because they exhibit the range of variability in the spatial distribution throughout the time series.

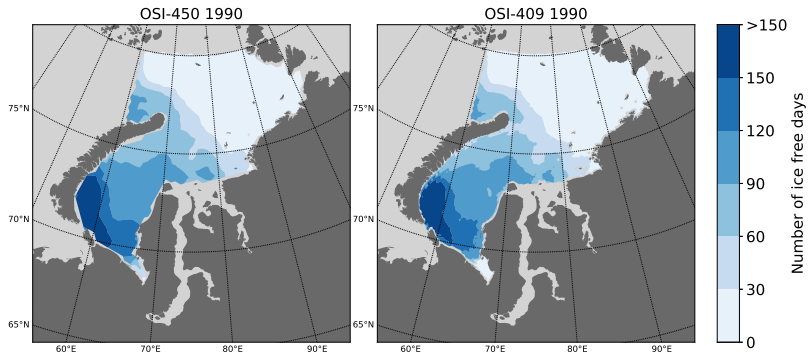

Figure 4.13: Annual ice free days from OSI-450 (center) and OSI-409 (right) datasets in 1990.

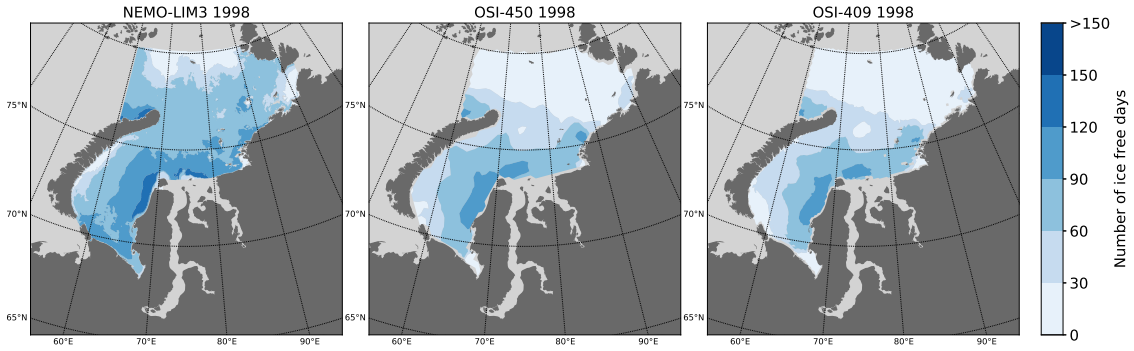

Figure 4.14: Annual ice free days from NEMO-LIM3 model (left), OSI-450 (center) and OSI-409 (right) datasets in 1998.

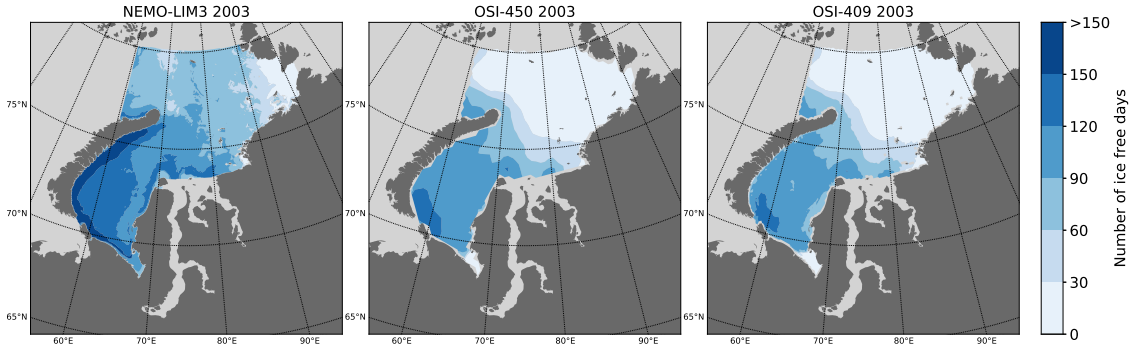

Figure 4.15: Annual ice free days from NEMO-LIM3 model (left), OSI-450 (center) and OSI-409 (right) datasets in 2003.

In general the number of ice free days is lowest in the northern and northeastern parts of the sea, where usually less than 30 per year are ice free. The highest number

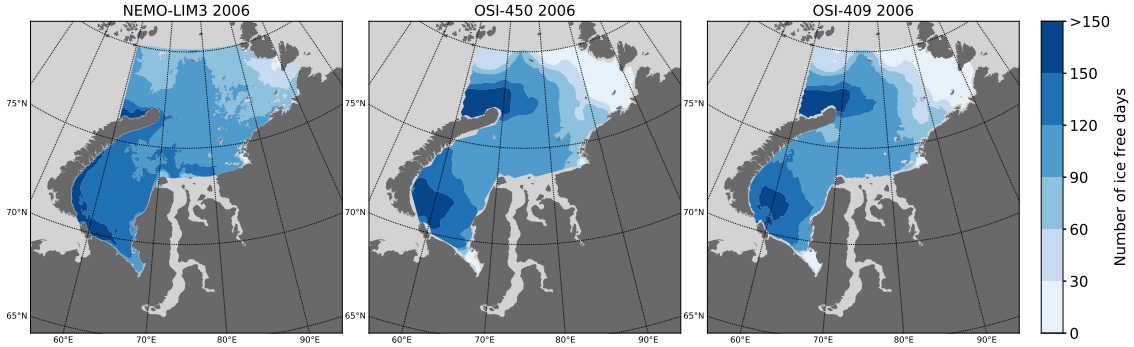

Figure 4.16: Annual ice free days from NEMO-LIM3 model (left), OSI-450 (center) and OSI-409 (right) datasets in 2006.

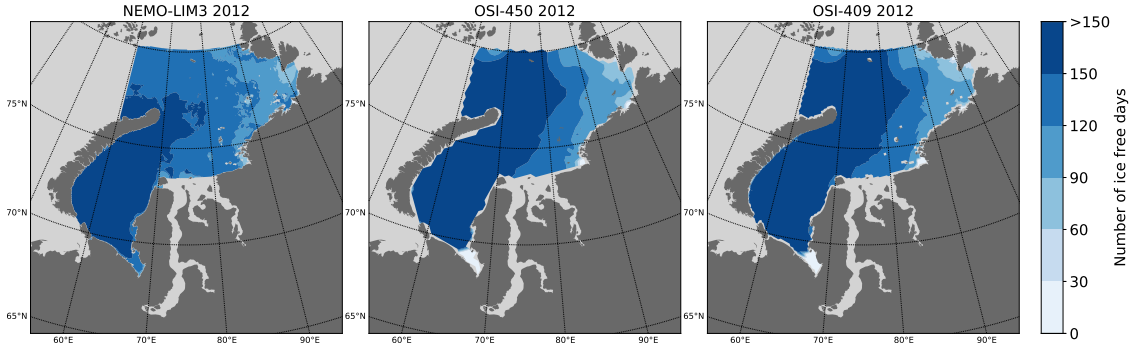

Figure 4.17: Annual ice free days from NEMO-LIM3 model (left), OSI-450 (center) and OSI-409 (right) datasets in 2012.

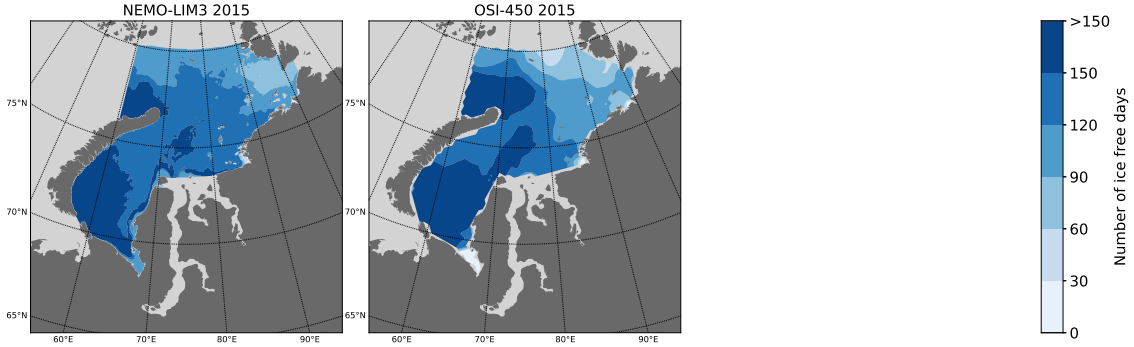

Figure 4.18: Annual ice free days from NEMO-LIM3 model (left) and OSI-450 (center) dataset in 2015.

of ice free days is found in the southern basin near Kara Gate and in the area north of Novaya Zemlya. The annual ice free time is regularly above 150 days in those two areas. Years with low overall ice free time took place in the earlier half of the

time series. In 1990 the number of ice free days was less than 120 everywhere in the Kara Sea while in 2012 there were less than 120 ice free days only near the coasts of Taimyr Peninsula and Severnaya Zemlya. The ice free time in the Kara Sea has been studied by *Rodrigues* (2008), who presents the distribution of the length of the ice free season in year 2006. The distribution of ice free time from 2006 in Figure 4.16 is consistent with the findings of (*Rodrigues*, 2008, Fig. 18).

The spatial distribution of ice free time has large interannual variations that can be explained by dynamic processes. During some years the ice free time is longer along shores if more polynyas are formed by offshore winds. In the southern Kara Sea the opposing shores of Yamal Peninsula and Novaya Zemlya can have shortened or elongated ice free seasons, respectively, depending on the direction of the prevailing winds. For example during years 1990, 2003 and 2006 ice is packed more in the east along the shores of Yamal Peninsula, while in 1998 the ice is pushed towards Novaya Zemlya in the west causing there a reduction in the annual ice free time.

The ice model simulation captures the variations in ice free time with relatively good accuracy. The general spatial distribution of ice free days is similar in both ice model and observed data. Years 2012 and 2015 are an example of the ice model giving very closely matching results compared to the observed datasets. In some years problems limited to certain regions are lowering the accuracy. The ice free time is generally shorter north of Novaya Zemlya in the ice model compared to observations possibly as a result of lower oceanic and atmospheric heat transport from the Barents Sea. The difference is visible for example in year 2006, when the area with more than 150 ice free days is very small in the model compared to the observed data. Near Kara Gate, where also the heat transport from the Barents Sea affects ice conditions, the model and observations are closer to each other than in the northern Kara Sea. In some years (1998, 2003) the ice model

data has significantly more ice free days than the satellite based datasets in the area in the central north, between 70...80°N and 70...90°E. The difference could be explained by smaller ice coverage in the summertime in the model compared to what is observed. The September ice area in sector N (Fig. 4.10) is much lower in the ice model data compared to the observed dataset both in 1998 and 2003. In the northeast near Severnaya Zemlya archipelago and along the coast of Taimyr Peninsula, the model often overestimates the number of ice free days (for example in 1998 and 2008). The difference could arise from the region being covered by fast ice, which is not accurately simulated in the ice model. As the formation of fast ice by arching between islands is not possible in the ice model, the ice can easily be pushed away from the shores leading to longer annual ice free time in such areas. Another possible explanation could be biases in atmospheric forcing in the coastal areas.

Figure 4.19 shows the spatial distribution of the trends of annual ice free time. The trends are calculated for each grid cell for the period 1997-2015. The ice free time is increasing in all datasets all across the Kara Sea. The strongest trends are found in the observed data in the region north of Novaya Zemlya where the ice free time has extended by over 10 days/year. The trend is equivalent to the sea changing from ice covered all year round to completely ice free in about 35 years. High trends are also found in the south near the Kara Gate and along the eastern coast of Novaya Zemlya. The trends become gradually weaker toward the east, where trends between 0 to 4 days/year are prevalent. The trends are lowest along the coasts of Yamal Peninsula and Severnaya Zemlya where fast ice formations are typical. The observational datasets show a decrease in ice free time in part of the Baydaratskaya Bay, but the quality of the observational data there might be affected by surrounding land areas.

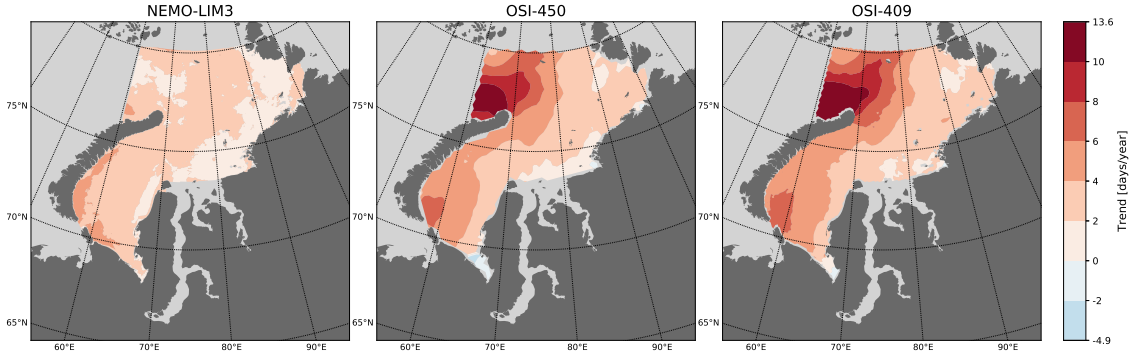

Figure 4.19: Trends in the annual number of ice free days calculated for the period 1997–2015 for each grid cell the NEMO-LIM3 model data (left) and satellite observation products OSI-450 (center) and OSI-409 (right).

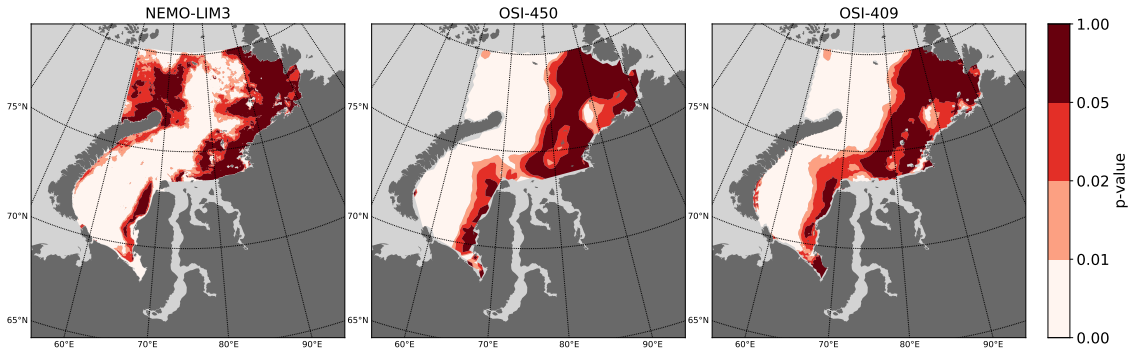

Figure 4.20: The statistical significance of the trends of Figure 4.19 expressed by the p-value. Trends in the areas with p-value over 0.05 (darkest red) are not statistically significant at 95% confidence level.

The p-value of the trends denoting the statistical significance is shown in Figure 4.20. The trends are statistically significant at 95% confidence level when the p-value is below 0.05, i.e. in the areas with white color in the figure. The trends are statistically significant on the western side of the Kara Sea where also the strongest trends took place. In the east, closer to the shores of Yamal and Taimyr Peninsulas and southwest of Severnaya Zemlya, trends are in general not statistically significant. This is caused by trends being small in comparison to the variability in the time series.

The trends in the ice model are greatly underestimated in the region affected by the oceanic heat transport from the Barents Sea. North of Novaya Zemlya, where the observed data has the largest trends, the ice model shows statistically not significant trends of only 0 to 4 days/year. For the other parts of the Kara Sea the results from the ice model and observational data are similar.

The trends are much higher than what *Rodrigues* (2008) has reported for the Kara Sea. The highest increase in the length of ice free season reported by *Rodrigues* was 80 days between 1979–2006, roughly equal to 3 days/year. Even though the number of ice free days is not directly comparable with the length of ice free season, these quantities only differ in the filtering of isolated ice free and ice covered days. It is very unlikely that such a big difference between Rodrigues' and our results would be caused by the different definitions of the quantities, or the differences in passive microwave datasets and processing algorithms. Since (*Rodrigues*, 2008, Fig. 18) only analyzed data until 2006, a more natural reason is that the lengthening of the ice free time has accelerated from the period 1979–2006 to the more recent period, 1997–2005.

5. Discussion

The results presented in section 4 clearly show a general trend toward a sea ice regime with less extensive, thinner and shorter living ice cover in the Kara Sea. The trends are apparent in both long term (1978–2015) and short term (1997–2015) time series in all variables in all subregions. The changes have been fastest near the edges of the Barents Sea, which is in agreement with multiple studies showing quick changes in the same area (*Li et al.*, 2017; *Onarheim and Årthun*, 2017). The decline in ice covered fraction or extent, thinning of the sea ice and the lengthening of the ice free season are also in general agreement with earlier studies (e.g. *Chen et al.*, 2016; *Rodrigues*, 2008; *Lang et al.*, 2017).

The decline in March and December ice covered fraction in the whole Kara Sea shown in Figure 4.5 can be attributed to the quick decline in sectors N and S (Figs. 4.8 and 4.11), where the effect of oceanic and atmospheric heat transport from the Barents Sea is strongest. In sectors C and F, the wintertime changes are slower and variability is smaller.

The decline of sea ice in the Barents Sea and the Kara Sea is due to an increase of ocean heat transport from the Barents Sea (e.g. *Li et al.*, 2017; *Årthun et al.*, 2012) and changes in atmospheric heat advection (e.g. *Sato et al.*, 2014). Increased heat flux from the Atlantic water transport could explain the quick retreat of ice cover in the northern Kara Sea. The warm water from the Barents Sea enters the Kara Sea through the opening between Novaya Zemlya and Franz Josef Land, where

the added heat leads to a reduction in ice covered area fraction and to more ice free days. The same effect is seen to a lesser extent in the southern Kara Sea, where warm water from the Barents Sea can be transported through the Kara Gate strait. The Novaya Zemlya islands effectively block the warm water from the Barents Sea entering the central parts of the Kara Sea and the changes in the wintertime ice conditions in the central and eastern Kara Sea are moderate (e.g. Fig. 4.19).

Warming of the atmosphere over the Kara Sea is a main factor for the loss of sea ice. The atmosphere in the Arctic is warming at an accelerated rate and most of the loss of sea ice in the Arctic can be attributed to the warming atmosphere. The actual effect of atmospheric warming on sea ice can differ because of the feedback effects associated with decline of sea ice. As the ice covered fraction in the Kara Sea decreases, the average surface albedo, surface heat fluxes and the conditions in the atmospheric boundary layer all change and affect the heat balance.

In summertime (June, September) all sectors contribute quite equally to the decline in ice covered fraction in the Kara Sea. The atmospheric radiative heat fluxes dominate in summertime because of increased amount of sun light and higher atmospheric temperature than in other seasons. The difference between subregions might be smaller in summertime because of the relatively small contribution of the ocean heat in the total heat budget at the ocean–sea ice–atmosphere interface. One can assume that when surface temperatures and amount of sun's radiation increase to dominate the total heat fluxes in summer, the heat balance in sectors N and S is closer to what it is in sectors C and F despite differences in ocean heat transport.

The difference in the sea ice concentration trends between observed datasets and the sea ice–ocean model is the biggest in the sectors connected to the Barents Sea. The low trend in sea ice–ocean model compared to the observations in Figures 4.5a and 4.5d can be attributed to underestimated trends in sectors N and S (Figs. 4.8 and 4.11). The accuracy of the ice model in sectors N and S is better in June or

September (Figs. 4.9 and 4.10) when the oceanic and atmospheric heat transport is contributing relatively less to the total heat budget than in other seasons. In the same regions the annual ice free time is underestimated (Fig. 4.19). The discrepancy between model and observations in the two sectors is likely caused by a shortcoming of the model simulating a too low heat transport from the Barents Sea to the Kara Sea. In addition shortcomings and biases in the atmospheric forcing data could greatly reduce model accuracy in the area.

In sectors C and F the effects of atmospheric forcing on ice conditions are relatively larger than in sectors N and S. The atmospheric forcing data used in the NEMO-LIM3 model setup is not entirely independent of observations (Sec. 3.1), which can explain the similarity of the model and observation results in sectors C and F. The weak oceanic and atmospheric heat transport in the model can also give a hint of what the ice conditions in the Kara Sea could be like if heat advection had smaller effect on the northern Kara Sea's ice conditions. The modeled decrease in ice covered fraction and extension of ice free time are more moderate than what is observed.

The interannual variability of the ice covered fraction has increased in winter months, but has reduced in summer months as a result of decline in the ice covered area. The phenomenon has been found and explained by *Goosse et al.* (2009). If the sea is completely ice covered even during an average year, an anomalously cold year would have no effect on ice covered fraction, as the area covered by ice cannot increase anymore. Similarly if the ice covered fraction is on average close to zero, an anomalously warm year would have a very minimal effect on the already small ice covered fraction. The variability in ice covered fraction is highest when the sea is on average partially ice covered. The ice area can then be higher during anomalously cold years and lower during anomalously warm years. The variations in the forcing

may remain unchanged, but the response of the ice cover changes depending on the relative extent of the ice cover in the sea.

In many months the interannual variations in ice covered fraction, thickness and ice free time are high and they reduce the statistical significance of trends in the time series. During the melting and freeze-up periods the interannual variability of the mean ice covered fraction is high throughout the time series (Figs. 4.6b and 4.6d). The high variability can be explained by great sensitivity of changing ice cover to varying external forcing during freeze-up and melt. The onset and progression of freeze-up is dependent on the heat stored during the open water season and the weather patterns affecting the ocean cooling and breaking and drifting of the new thin ice. In the melting season the thickness of sea ice, ice–albedo feedbacks and heat fluxes all affect the pace of melting.

The anomalies in the monthly mean ice covered fractions have a multitude of possible explanations. The anomalies in the ice conditions are explained by variations in the atmospheric and oceanic conditions. There is a multitude of phenomena that can lead to anomalous sea ice extent, thickness and ice free time. The strongest anomalies are likely a sum of many phenomena acting at the same time.

The years with anomalously low ice covered fraction can be caused by passing cyclones and variations in the large scale atmospheric pressure field. The cyclones bring with them warm air, which can significantly change the heat fluxes at the sea ice–atmosphere interface. Blocking pressure cells acting in the region can have the opposite effect. The cyclonic winds can mix the ocean waters and cause melting at the ice bottom and open leads in the ice cover, changing the surface albedo and surface heat fluxes.

Variations in volume and temperature of transported ocean water, river inflow, as well as stratification of the water column, have a strong effect on sea ice. They change the heat balance at the sea ice–ocean interface and heat content in the

ocean mixing layer, which influence the melting and freezing of the sea ice. In the northern parts the Kara Sea ice transport can also have substantial effect on the ice covered fraction. The sea ice export volumes to the Arctic ocean vary with a possible correlation with the climatic indexes, such as AO, NAO and DA.

The general thinning of sea ice makes extremely low ice extents more likely. The thin ice melts faster, moves faster, and can be easily broken down, which extends the open water season and increases the total heat accumulation in the ocean mixing layer during the summertime. In the next winter the ice freeze-up may be delayed because more energy has to be released in order to cool down the ocean.

The NEMO-LIM3 coupled sea ice–ocean model captured the changes and variability of the ice conditions well. The anomalies in ice covered fraction are well correlated with the observational data (Fig. 4.6). The variability of annual ice free time is generally well captured by the sea ice–ocean model (Figs. 4.13–4.18). This suggests that the model's responses to varying atmospheric and oceanic forcings are well represented, although good correlation can be caused by observations constraining the model as shown in Section 3.1. Further attention is required in order to fix the potential problem with the ocean heat transport, that greatly affects the model data quality in the northern Kara Sea. The melting of the sea ice in summer is too quick in the ice model, but it could be improved with ice albedo adjustments. As pointed out, the ice cover is in a very sensitive phase during melting and already small differences in the simulation can lead to considerable differences in the sea ice covered fraction. It could be possible to improve the accuracy of the ice model in the proximity of shores with a more detailed simulation of fast ice. The simulation of fast ice formation by arching would, however, require a specific version of EVP rheology (*Beatty and Holland*, 2010), or an entirely different rheology (*Olason*, 2016).

The overall decline and thinning of the ice cover is making marine traffic in the Kara Sea easier and more accessible. The fast decrease in the ice concentrations in the northern parts of the Kara Sea could make the northern options for the Northern Sea Route preferred over the options following close to the shoreline. Since the ice concentrations around Severnaya Zemlya have remained high because of stable fast ice formations, it is possible the in coming years and decades the routes north of Severnaya Zemlya will become preferable over the routes traversing the Vilkitsky Strait. Simulated ice free time at shores of Severnaya Zemlya has been higher than observed (Sec. 4.5), which is problematic for navigation planning.

The large variations in the ice cover should be taken into account when planning any maritime operations. The variability of the ice covered fraction and thickness is high in autumn, winter and spring. The high variability means that, despite the changing ice regime, extreme ice conditions are likely to occur from year to year. In subregional scales the variability of ice covered fraction during months of partial ice cover can be amplified by drifting of sea ice. Depending on the direction of winds and currents, the ice could be transported from one subregion to another. Because of the large variability, using ice data from only one or few years for decision making should also be avoided as ice conditions in one single year will likely not represent the current state of the sea ice system. From the perspective of forecasting ice conditions in the Kara Sea, the increased variability in winter time makes it harder to predict ice conditions. In the summertime, the high season for marine traffic in the region, the decrease in ice covered fraction variability should make it easier to accurately predict ice conditions.

It should be noted, that the time series from the model simulation period (1997–2015) are relatively short for climate studies. Generally 30 years has been accepted as the minimum length of a time series to give an estimate of climatic trends with high enough confidence. For example, the trends of ice free time (Fig. 4.19) and

ice thickness (Fig. 4.12) presented here show the relatively short term changes that can be subject to various natural oscillations. The time series from the beginning of the satellite observation era to present day, like in the ice covered fraction figures (Fig. 4.5), are long enough to confidently represent changes in climate.

The work done in the thesis could be continued by studying in detail the heat fluxes at the Kara Sea boundaries and on the sea ice–ocean and sea ice–atmosphere interface. The freshwater storage and stratification of the sea can also influence the sea ice variability and changes and should be studied for a full explanation of the events leading to the decline of sea ice. Better river runoff data is also required for a more realistic simulation. This could help to better quantify the reasons behind the changes and variability in the ice cover studied in this thesis, and support current qualitative arguments. Extending the time series from model simulations to cover the years since the start of the satellite observed sea ice data would improve the confidence of the simulation dataset. Extending the sea ice concentration datasets to more recent years would be valuable as it would show whether the extreme changes are still ongoing.

6. Conclusions

The changes and interannual variability of the ice conditions in the Kara Sea were studied in this thesis. In addition, the accuracy of model simulation was compared with the observational data in order to validate the ice model. For the analysis, simulation data from the coupled sea ice–ocean model NEMO-LIM3.6 for the Kara Sea was used together with two EUMETSAT OSI-SAF satellite observation based sea ice concentration datasets.

The simulation with the NEMO-LIM3.6 ice model in the Kara Sea revealed promising results. The trends of ice covered fraction from the simulation are similar to those found in observational data, although they are in many cases slightly underestimated. The anomalies in ice covered fraction are well correlated between the simulation and observational data. The model setup had an problem with oceanic and atmospheric heat transported to the Kara Sea from the Barents Sea, which lead to overestimated ice concentrations in the northern Kara Sea. When the problem in the model is corrected, its development toward operational use can be continued with a good confidence.

The warming atmosphere and the ocean heat transport from the Barents Sea, together with various feedback effects, are leading to a loss of sea ice in all respects. The ice covered fraction of the Kara Sea and its subregions has shrunk at least since 1979. In shorter term, since 1997, the Kara Sea has become ice free for a longer part of the year, and the mean sea ice thickness has decreased in all months. The

changes are fastest in the areas north of Novaya Zemlya, where the influence of heat transport with ocean currents and main storm track from the Barents Sea are the main driving factors for the change. In the eastern half of the Kara Sea the changes of the ice conditions are slower.

The variability of sea ice covered fraction in the Kara Sea is in many months high and reduces significance of trends found in the time series. Changes in variability are related to the relative extent of the ice cover. The variability is increasing in winter months and decreasing in summer months.

The ice regime in the Kara Sea is changing fast. Based on climate model scenarios, the ice conditions have become more variable and the ice season is becoming shorter and milder. The ice regime shift is likely to continue in the future with the continuing warming of the Arctic.

Acknowledgements

Funding for this thesis came from the KAMON project, funded through the Academy of Finland's Arctic Research Programme (ARKTIKO), and from a scholarship granted by Merenkulun säätiö.

I would like to thank the supervisors, Andrea Gierisch and Jari Haapala, for their feedback and support throughout the thesis writing and analysis process. I also thank Mikko Lensu, Eero Rinne, Robinson Hordoir, Igor Polyakov, Matti Leppäranta and Petteri Uotila for all suggestions and assistance they have provided.

Bibliography

Amante, C., and B. Eakins (2009), ETOPO1 1 arc-minute global relief model: Procedures, data sources and analysis. NOAA technical memorandum NESDIS NGDC-24., doi:10.7289/V5C8276M.

Årthun, M., T. Eldevik, L. H. Smedsrud, Skagseth, and R. B. Ingvaldsen (2012), Quantifying the influence of Atlantic heat on Barents Sea ice variability and retreat, *Journal of Climate*, *25*(13), 4736–4743, doi:10.1175/JCLI-D-11-00466.1.

Barber, D. G., W. N. Meier, G. S., C. J. Mundy, H. M., S. Kern, Z. Li, C. Michel, D. K. Perovich, and T. Tamura (2017), Chapter 5. Arctic sea ice, in *Ice and Permafrost in the Arctic (SWIPA) 2017*, pp. 104–127, Arctic Monitoring and Assessment Programme (AMAP), Oslo, Norway, retrieved from `https://www.amap.no/documents/download/1448`.

Barnier, B., G. Madec, T. Penduff, J.-M. Molines, A.-M. Treguier, J. Le Sommer, A. Beckmann, A. Biastoch, C. Böning, J. Dengg, et al. (2006), Impact of partial steps and momentum advection schemes in a global ocean circulation model at eddy-permitting resolution, *Ocean Dynamics*, *56*(5-6), 543–567, doi:10.1007/s10236-006-0082-1.

Beatty, C. K., and D. M. Holland (2010), Modeling Landfast Sea Ice by Adding Tensile Strength, *Journal of Physical Oceanography*, *40*(1), 185–198, doi:10.1175/2009JPO4105.1.

Bintanja, R., E. C. van der Linden, and W. Hazeleger (2012), Boundary layer stability and Arctic climate change: a feedback study using EC-Earth, *Climate Dynamics*, *39*(11), 2659–2673, doi:10.1007/s00382-011-1272-1.

Boisvert, L. N., A. A. Petty, and J. C. Stroeve (2016), The impact of the extreme winter 2015/16 Arctic cyclone on the Barents–Kara Seas, *Monthly Weather Review*, *144*(11), 4279–4287, doi:10.1175/MWR-D-16-0234.1.

Boé, J., A. Hall, and X. Qu (2009), Current GCMs' Unrealistic Negative Feedback in the Arctic, *Journal of Climate*, *22*(17), 4682–4695, doi:10.1175/2009JCLI2885.1.

Buixadé Farré, A., S. R. Stephenson, L. Chen, M. Czub, Y. Dai, D. Demchev, Y. Efimov, P. Graczyk, H. Grythe, K. Keil, N. Kivekäs, N. Kumar, N. Liu, I. Matelenok, M. Myksvoll, D. O'Leary, J. Olsen, S. Pavithran.A.P, E. Petersen, A. Raspotnik, I. Ryzhov, J. Solski, L. Suo, C. Troein, V. Valeeva, J. van Rijckevorsel, and J. Wighting (2014), Commercial Arctic shipping through the Northeast Passage: Routes, resources, governance, technology, and infrastructure, *Polar Geography*, *37*(4), 298–324, doi:10.1080/1088937X.2014.965769.

Cavalieri, D. J., and C. L. Parkinson (2012), Arctic sea ice variability and trends, 1979–2010, *The Cryosphere*, *6*(4), 881–889, doi:10.5194/tc-6-881-2012.

Chen, H. W., R. B. Alley, and F. Zhang (2016), Interannual Arctic sea ice variability and associated winter weather patterns: A regional perspective for 1979–2014, *Journal of Geophysical Research: Atmospheres*, *121*(24), 14,433–14,455, doi:10.1002/2016JD024769, 2016JD024769.

Comiso, J. C. (1986), Characteristics of Arctic winter sea ice from satellite multispectral microwave observations, *Journal of Geophysical Research: Oceans*, *91*(C1), 975–994, doi:10.1029/JC091iC01p00975.

Comiso, J. C. (2012), Large decadal decline of the Arctic multiyear ice cover, *Journal of Climate*, *25*(4), 1176–1193, doi:10.1175/JCLI-D-11-00113.1.

Comiso, J. C., C. L. Parkinson, R. Gersten, and L. Stock (2008), Accelerated decline in the Arctic sea ice cover, *Geophysical Research Letters*, *35*(1), doi:10.1029/2007GL031972, l01703.

Dee, D. P., S. M. Uppala, A. J. Simmons, P. Berrisford, P. Poli, S. Kobayashi, U. Andrae, M. A. Balmaseda, G. Balsamo, P. Bauer, P. Bechtold, A. C. M. Beljaars, L. van de Berg, J. Bidlot, N. Bormann, C. Delsol, R. Dragani, M. Fuentes, A. J. Geer, L. Haimberger, S. B. Healy, H. Hersbach, E. V. Hólm, L. Isaksen, P. Kållberg, M. Köhler, M. Matricardi, A. P. McNally, B. M. Monge-Sanz, J.-J. Morcrette, B.-K. Park, C. Peubey, P. de Rosnay, C. Tavolato, J.-N. Thépaut, and F. Vitart (2011), The ERA-Interim reanalysis: Configuration and performance of the data assimilation system, *Quarterly Journal of the Royal Meteorological Society*, *137*(656), 553–597, doi:10.1002/qj.828.

Divine, D. V., R. Korsnes, and A. Makshtas (2003), Variability and climate sensitivity of fast ice extent in the north-eastern Kara Sea, *Polar Research*, *22*(1), 27–34, doi:10.3402/polar.v22i1.6440.

Divine, D. V., R. Korsnes, and A. P. Makshtas (2004), Temporal and spatial variation of shore-fast ice in the Kara Sea, *Continental Shelf Research*, *24*(15), 1717 – 1736, doi:10.1016/j.csr.2004.05.010.

Divine, D. V., R. Korsnes, A. P. Makshtas, F. Godtliebsen, and H. Svendsen (2005), Atmospheric-driven state transfer of shore-fast ice in the northeastern Kara Sea, *Journal of Geophysical Research: Oceans*, *110*(C9), doi:10.1029/2004JC002706, c09013.

Dussin, R., B. Barnier, and L. Brodeau (2016), The making of Drakkar forcing set DFS5, retrieved from `https://www.drakkar-ocean.eu/publications/reports/report_DFS5v3_April2016.pdf`.

Eastwood, S., M. Jenssen, T. Lavergne, A. M. Sørensen, and R. Tonboe (2017), Global sea ice concentration reprocessing, product user manual, product OSI-409, OSI-409-a, OSI-430, document version 2.5, data set version 1.2, retrieved from `http://osisaf.met.no/docs/osisaf_cdop3_ss2_pum_sea-ice-conc-reproc_v2p5.pdf`.

Egbert, G. D., and S. Y. Erofeeva (2002), Efficient inverse modeling of barotropic ocean tides, *Journal of Atmospheric and Oceanic Technology*, *19*(2), 183–204, doi:10.1175/1520-0426(2002)019<0183:EIMOBO>2.0.CO;2.

EUMETSAT Ocean and Sea Ice Satellite Application Facility (2015), Global sea ice concentration climate data records 1978-2015 (v1.2, 2015), [online], doi:10.15770/EUM_SAF_OSI_0001 and 10.15770/EUM_SAF_OSI_0005.

EUMETSAT Ocean and Sea Ice Satellite Application Facility (2017), Global sea ice concentration climate data record 1979-2015 (v2.0, 2017), [online], doi:10.15770/EUM_SAF_OSI_0008.

Ghatak, D., and J. Miller (2013), Implications for Arctic amplification of changes in the strength of the water vapor feedback, *Journal of Geophysical Research: Atmospheres*, *118*(14), 7569–7578, doi:10.1002/jgrd.50578.

Goosse, H., O. Arzel, C. M. Bitz, A. de Montety, and M. Vancoppenolle (2009), Increased variability of the Arctic summer ice extent in a warmer climate, *Geo-*

physical Research Letters, *36*(23), doi:10.1029/2009GL040546, l23702.

Hanzlick, D., and K. Aagaard (1980), Freshwater and Atlantic water in the Kara Sea, *Journal of Geophysical Research: Oceans*, *85*(C9), 4937–4942, doi:10.1029/JC085iC09p04937.

Harms, I. H., and M. J. Karcher (1999), Modeling the seasonal variability of hydrography and circulation in the Kara Sea, *Journal of Geophysical Research: Oceans*, *104*(C6), 13,431–13,448, doi:10.1029/1999JC900048.

Hibler III, W. D. (1979), A dynamic thermodynamic sea ice model, *Journal of Physical Oceanography*, *9*(4), 815–846, doi:10.1175/1520-0485(1979)009<0815:ADTSIM>2.0.CO;2.

Hunke, E. C., and J. K. Dukowicz (1997), An elastic–viscous–plastic model for sea ice dynamics, *Journal of Physical Oceanography*, *27*(9), 1849–1867, doi:10.1175/1520-0485(1997)027<1849:AEVPMF>2.0.CO;2.

IPCC (2014), Climate Change 2014: Synthesis Report. Contribution of Working Groups I, II and III to the Fifth Assessment Report of the Intergovernmental Panel on Climate Change [Core Writing Team, R.K. Pachauri and L.A. Meyer (eds.)], IPCC, Geneva, Switzerland, 151 pp.

Johannessen, O., V. Alexandrov, I. Frolov, S. Sandven, L. Pettersson, L. Bobylev, K. Kloster, V. Smirnov, Y. Mironov, and N. Babich (2006), *Remote Sensing of Sea Ice in the Northern Sea Route: Studies and Applications*, Springer Praxis Books, 1st ed., 472 pp., Springer-Verlag, Berlin.

Jung, O., M.-K. Sung, K. Sato, Y.-K. Lim, S.-J. Kim, E.-H. Baek, J.-H. Jeong, and B.-M. Kim (2017), How does the SST variability over the western North Atlantic Ocean control Arctic warming over the Barents–Kara Seas?, *Environmental Research Letters*, *12*(3), 034,021, doi:10.1088/1748-9326/aa5f3b.

Kern, S., I. Harms, S. Bakan, and Y. Chen (2005), A comprehensive view of Kara Sea polynya dynamics, sea-ice compactness and export from model and remote sensing data, *Geophysical Research Letters*, *32*(15), doi:10.1029/2005GL023532, l15501.

Khon, V. C., I. I. Mokhov, and V. A. Semenov (2017), Transit navigation through Northern Sea Route from satellite data and CMIP5 simulations, *Environmental Research Letters*, *12*(2), 024,010, doi:10.1088/1748-9326/aa5841.

Kwok, R. (2000), Recent changes in Arctic Ocean sea ice motion associated with the North Atlantic Oscillation, *Geophysical Research Letters*, *27*(6), 775–778, doi:10.1029/1999GL002382.

Kwok, R., G. F. Cunningham, M. Wensnahan, I. Rigor, H. J. Zwally, and D. Yi (2009), Thinning and volume loss of the Arctic Ocean sea ice cover: 2003-2008, *Journal of Geophysical Research: Oceans*, *114*(C7), doi:10.1029/2009JC005312, c07005.

Lang, A., S. Yang, and E. Kaas (2017), Sea ice thickness and recent Arctic warming, *Geophysical Research Letters*, *44*(1), 409–418, doi:10.1002/2016GL071274.

Lei, R., H. Xie, J. Wang, M. Leppäranta, I. Jónsdóttir, and Z. Zhang (2015), Changes in sea ice conditions along the Arctic Northeast Passage from 1979 to 2012, *Cold Regions Science and Technology*, *119*, 132–144, doi:10.1016/j.coldregions.2015.08.004.

Leppäranta, M. (2011), *The Drift of Sea Ice*, Springer Praxis Books, 2nd ed., 350 pp., Springer Berlin Heidelberg, doi:10.1007/978-3-642-04683-4.

Li, D., R. Zhang, and T. R. Knutson (2017), On the discrepancy between observed and CMIP5 multi-model simulated Barents Sea winter sea ice decline, *Nature Communications*, *8*(14991), doi:10.1038/ncomms14991.

Meier, W. N., S. Gerland, M. A. Granskog, J. R. Key, C. Haas, G. K. Hovelsrud, K. M. Kovacs, A. Makshtas, C. Michel, D. Perovich, J. D. Reist, and B. E. H. van Oort (2011), Chapter 9. Sea Ice, in *Ice and Permafrost in the Arctic (SWIPA): Climate change and the cryosphere*, pp. 9:1–9:88, Arctic Monitoring and Assessment Programme (AMAP), Oslo, Norway, retrieved from `https://www.amap.no/documents/download/2987`.

Miles, M. W., D. V. Divine, T. Furevik, E. Jansen, M. Moros, and A. E. J. Ogilvie (2014), A signal of persistent Atlantic multidecadal variability in Arctic sea ice, *Geophysical Research Letters*, *41*(2), 463–469, doi:10.1002/2013GL058084, 2013GL058084.

Notz, D. (2014), Sea-ice extent and its trend provide limited metrics of model performance, *Cryosphere*, *8*(1), 229–243, doi:10.5194/tc-8-229-2014.

Notz, D., and M. G. Worster (2009), Desalination processes of sea ice revisited, *Journal of Geophysical Research: Oceans*, *114*(C5), doi:10.1029/2008JC004885,

c05006.

Oikkonen, A., and J. Haapala (2011), Variability and changes of Arctic sea ice draft distribution - submarine sonar measurements revisited, *Cryosphere*, *vol. 5*(no. 4), pp. 917–929, doi:10.5194/tc-5-917-2011.

Olason, E. (2016), A dynamical model of Kara Sea land-fast ice, *Journal of Geophysical Research: Oceans*, *121*(5), 3141–3158, doi:10.1002/2016JC011638.

Onarheim, I. H., T. Eldevik, M. Årthun, R. B. Ingvaldsen, and L. H. Smedsrud (2015), Skillful prediction of Barents Sea ice cover, *Geophysical Research Letters*, *42*(13), 5364–5371, doi:10.1002/2015GL064359.

Onarheim, I. H., and M. Årthun (2017), Toward an ice-free Barents Sea, *Geophysical Research Letters*, *44*(16), 8387–8395, doi:10.1002/2017GL074304.

Overland, J. E., and M. Wang (2013), When will the summer Arctic be nearly sea ice free?, *Geophysical Research Letters*, *40*(10), 2097–2101, doi:10.1002/grl.50316.

Overland, J. E., M. Wang, J. E. Walsh, and J. C. Stroeve (2014), Earth's Future Future Arctic climate changes: Adaptation and mitigation time scales, *2*(2), 68–74, doi:10.1002/2013EF000162.

Panteleev, G., A. Proshutinsky, M. Kulakov, D. A. Nechaev, and W. Maslowski (2007), Investigation of the summer Kara Sea circulation employing a variational data assimilation technique, *Journal of Geophysical Research: Oceans*, *112*(C4), doi:10.1029/2006JC003728, c04S15.

Parkinson, C. L., and D. J. Cavalieri (2008), Arctic sea ice variability and trends, 1979-2006, *Journal of Geophysical Research: Oceans*, *113*(C7), doi:10.1029/2007JC004558, c07003.

Persson, O., and T. Vihma (2016), The atmosphere over sea ice, in *Sea Ice*, edited by D. Thomas, 3rd ed., chap. 6, pp. 160–196, John Wiley & Sons, Incorporated, Hoboken.

Petrich, C., and H. Eicken (2016), Overview of sea ice growth and properties, in *Sea Ice*, edited by D. Thomas, 3rd ed., chap. 1, pp. 1–41, John Wiley & Sons, Incorporated, Hoboken.

Polyakov, I. V., G. V. Alekseev, R. V. Bekryaev, U. S. Bhatt, R. Colony, M. A. Johnson, V. P. Karklin, D. Walsh, and A. V. Yulin (2003), Long-term ice variability in

Arctic marginal seas, *Journal of Climate*, *16*(12), 2078–2085, doi:10.1175/1520-0442(2003)016<2078:LIVIAM>2.0.CO;2.

Polyakov, I. V., A. V. Pnyushkov, M. B. Alkire, I. M. Ashik, T. M. Baumann, E. C. Carmack, I. Goszczko, J. Guthrie, V. V. Ivanov, T. Kanzow, et al. (2017), Greater role for atlantic inflows on sea-ice loss in the eurasian basin of the arctic ocean, *Science*, *356*(6335), 285–291, doi:10.1126/science.aai8204.

Rampal, P., J. Weiss, and D. Marsan (2009), Positive trend in the mean speed and deformation rate of Arctic sea ice, 1979–2007, *Journal of Geophysical Research: Oceans*, *114*(C05013), doi:10.1029/2008JC005066.

Rigor, I. G., J. M. Wallace, and R. L. Colony (2002), Response of sea ice to the Arctic Oscillation, *Journal of Climate*, *15*(18), 2648–2663, doi:10.1175/1520-0442(2002)015<2648:ROSITT>2.0.CO;2.

Rodrigues, J. (2008), The rapid decline of the sea ice in the Russian Arctic, *Cold Regions Science and Technology*, *54*(2), 124–142, doi:10.1016/j.coldregions.2008.03.008.

Rodrigues, J. (2009), The increase in the length of the ice-free season in the Arctic, *Cold Regions Science and Technology*, *59*(1), 78–101, doi:10.1016/j.coldregions.2009.05.006.

Rogers, J. C., and H. Van Loon (1979), The seesaw in winter temperatures between Greenland and northern Europe. Part II: Some oceanic and atmospheric effects in middle and high latitudes, *Monthly Weather Review*, *107*(5), 509–519.

Rothrock, D. A., Y. Yu, and G. A. Maykut (1999), Thinning of the Arctic sea-ice cover, *Geophysical Research Letters*, *26*(1), 3469–3472, doi:10.1029/1999GL010863.

Rousset, C., M. Vancoppenolle, G. Madec, T. Fichefet, S. Flavoni, A. Barthélemy, R. Benshila, J. Chanut, C. Lévy, S. Masson, and F. Vivier (2015), The Louvain-La-Neuve sea ice model LIM3.6: Global and regional capabilities, *Geoscientific Model Development*, *8*(10), 2991– 3005, doi:10.5194/gmd-8-2991-2015.

Sato, K., J. Inoue, and M. Watanabe (2014), Influence of the Gulf Stream on the Barents Sea ice retreat and Eurasian coldness during early winter, *Environmental Research Letters*, *9*(8), 084,009, doi:10.1088/1748-9326/9/8/084009.

Screen, J. A., and I. Simmonds (2010), The central role of diminishing sea ice in recent Arctic temperature amplification, *Nature*, *464*, 1334–1337, doi:10.1038/nature09051.

Serreze, M. C., M. M. Holland, and J. Stroeve (2007), Perspectives on the Arctic's shrinking sea-ice cover, *Science*, *315*(5818), 1533–1536, doi:10.1126/science.1139426.

Serreze, M. C., A. P. Barrett, J. C. Stroeve, D. N. Kindig, and M. M. Holland (2009), The emergence of surface-based Arctic amplification, *The Cryosphere*, *3*(1), 11–19, doi:10.5194/tc-3-11-2009.

Simmonds, I. (2015), Comparing and contrasting the behaviour of Arctic and Antarctic sea ice over the 35 year period 1979-2013, *Annals of Glaciology*, *56*(69), 18–28, doi:10.3189/2015AoG69A909.

Smith, D. M. (1996), Extraction of winter total sea-ice concentration in the Greenland and Barents Seas from SSM/I data, *International Journal of Remote Sensing*, *17*(13), 2625–2646, doi:10.1080/01431169608949096.

Sørensen, A. M., T. Lavergne, and S. Eastwood (2017), Global sea ice concentration climate data record, product user manual, product OSI-450, document version 1.0, data set version 2.0, doi:10.15770/EUM_SAF_OSI_0008.

Stroeve, J. C., J. Maslanik, M. C. Serreze, I. Rigor, W. Meier, and C. Fowler (2011), Sea ice response to an extreme negative phase of the Arctic Oscillation during winter 2009/2010, *Geophysical Research Letters*, *38*(2), doi:10.1029/2010GL045662, l02502.

Thompson, D. W. J., and J. M. Wallace (1998), The Arctic oscillation signature in the wintertime geopotential height and temperature fields, *Geophysical Research Letters*, *25*(9), 1297–1300, doi:10.1029/98GL00950.

Thorndike, A. S., D. A. Rothrock, G. A. Maykut, and R. Colony (1975), The thickness distribution of sea ice, *Journal of Geophysical Research*, *80*(33), 4501–4513, doi:10.1029/JC080i033p04501.

Tonboe, R. T., S. Eastwood, T. Lavergne, A. M. Sørensen, N. Rathmann, G. Dybkjaer, L. T. Pedersen, J. L. Høyer, and S. Kern (2016), The EUMETSAT sea ice concentration climate data record, *The Cryosphere*, *10*(5), 2275–2290, doi:10.5194/tc-10-2275-2016.

Vancoppenolle, M., T. Fichefet, H. Goosse, S. Bouillon, G. Madec, and M. A. M. Maqueda (2009), Simulating the mass balance and salinity of Arctic and Antarctic sea ice. 1. Model description and validation, *Ocean Modelling*, *27*(1), 33–53, doi:10.1016/j.ocemod.2008.10.005.

Vihma, T. (2014), Effects of Arctic Sea Ice Decline on Weather and Climate: A Review, *Surveys in Geophysics*, *35*(5), 1175–1214, doi:10.1007/s10712-014-9284-0.

Volkov, V., O. Johannessen, V. Borodachev, G. Voinov, L. Pettersson, L. Bobylev, and A. Kouraev (2002), *Polar Seas Oceanography: An integrated case study of the Kara Sea*, Springer Praxis Books, 1st ed., 450 pp., Springer-Verlag, Berlin.

Wang, J., J. Zhang, E. Watanabe, M. Ikeda, K. Mizobata, J. E. Walsh, X. Bai, and B. Wu (2009), Is the dipole anomaly a major driver to record lows in Arctic summer sea ice extent?, *Geophysical Research Letters*, *36*(5), doi:10.1029/2008GL036706, l05706.

Watanabe, E., J. Wang, A. Sumi, and H. Hasumi (2006), Arctic dipole anomaly and its contribution to sea ice export from the Arctic Ocean in the 20th century, *Geophysical Research Letters*, *33*(23), doi:10.1029/2006GL028112, l23703.

Wu, B., J. Wang, and J. E. Walsh (2006), Dipole anomaly in the winter Arctic atmosphere and its association with sea ice motion, *Journal of Climate*, *19*(2), 210–225, doi:10.1175/JCLI3619.1.